Impacts of Large-Scale Offshore Wind Farms on Tropical Cyclones: A Case Study of Typhoon Hato

PENGHUI ZHANG,[a] SHAOKUN DENG,[a] PENG-FEI TUO,[a] AND SHENGLI CHEN[a]

[a] *Institute for Ocean Engineering, Shenzhen International Graduate School, Tsinghua University, Shenzhen, China*

(Manuscript received 11 September 2023, in final form 17 June 2024, accepted 5 July 2024)

ABSTRACT: With the rising global demand for renewable energy sources, a great number of offshore wind farms are being built worldwide, as well as in the northern South China Sea. There is, however, limited research on the impact of offshore wind farms on the atmospheric and marine environment, particularly tropical cyclones, which frequently occur in summertime in the South China Sea. In this paper, we employ the Weather Research and Forecasting (WRF) Model to investigate the impacts of large-scale offshore wind farms on tropical cyclones, using the case of Typhoon Hato, which caused severe damage in 2017. Model results reveal that maximum wind speeds in coastal areas decrease by 3–5 m s^{-1} and can reach a maximum of 8 m s^{-1}. Furthermore, the wind farms change low-level moisture convergence, causing a shift in the precipitation center toward the wind farm area and causing a significant overall reduction (up to 16%) in precipitation. Model sensitivity experiments on the area and layout of the wind farm have been carried out. The results show that larger wind farm areas and denser turbine layouts cause a more substantial decrease in the wind speed over the coast and accumulated precipitation reduction, further corroborating our findings.

SIGNIFICANCE STATEMENT: This study holds significant implications for developing offshore wind farms in tropical cyclone-prone regions like the South China Sea. By focusing on Typhoon Hato as a case study, the research sheds light on the previously understudied relationship between large-scale offshore wind farms and tropical cyclones. The observed decrease in coastal wind speeds and altered precipitation patterns due to wind farm presence highlights the potential for mitigating cyclone-related risks in these regions. Additionally, the study's sensitivity experiments underscore the importance of careful planning and design in optimizing wind farm layouts for maximum impact reduction. This research contributes vital insights into sustainable energy infrastructure development while minimizing environmental and meteorological risks in cyclone-prone areas.

KEYWORDS: Tropical cyclones; Mesoscale models; Renewable energy

1. Introduction

Tropical cyclones, such as typhoons, are weather systems originating in tropical or subtropical ocean areas and can generate huge damages due to strong winds, storm surges, and rainfall-caused floods (Peduzzi et al. 2012; Zhang et al. 2009). Whether tropical cyclone activity has changed or will change in a warming climate is currently a matter of great public and scientific concern and is an important topic in the summarized scientific reports of the Intergovernmental Panel on Climate Change (IPCC) and in many review papers (IPCC 2007, 2014; Knutson et al. 2010, 2019, 2020; Sobel et al. 2016; Walsh et al. 2015, 2016). Guangdong Province of China is located in the northern part of the South China Sea (SCS) and experiences the landfall of three to four typhoons annually, making it one of China's most severely affected regions.

As a clean energy source, wind power has seen rapid growth in global installed capacity in recent years and will play an important role in combating climate change. For example, Guangdong Province plans to construct large-scale offshore wind farms in the northern part of the SCS. Large-scale wind farms may impact local climate or weather, and many researchers have conducted extensive research on this issue. Large-scale wind farms can alter the atmospheric boundary layer, enhance local vertical turbulent mixing, lead to changes in the surrounding surface temperature (Baidya Roy et al. 2004; Baidya Roy and Traiteur 2010; Fitch et al. 2013; Miller and Keith 2018; Platis et al. 2020; Shepherd et al. 2020; Wang et al. 2019), and attenuate the wind speed in the wind farm and downstream regions, which is also validated by observations (Cañadillas et al. 2020; Hasager et al. 2015; Schneemann et al. 2020). Furthermore, wind farms can also affect surface heat flux and water vapor exchange, indirectly altering other meteorological elements such as clouds and precipitation (Fiedler and Bukovsky 2011; Fitch 2015; Lauridsen and Ancell 2018).

Compared with the research on the impact of land-based wind farms, there is limited research regarding the impact of offshore wind farms. Jacobson et al. (2014) investigated the role of offshore wind farms during Hurricane Katrina and Hurricane Sandy. The results showed that offshore wind farms could reduce near-surface wind speeds during hurricanes and decrease storm surges by 6%–79%. Possner and Caldeira (2017) used an atmosphere–ocean fully coupled model to simulate large-scale wind farms on open oceans and on land and found that the wind speed at 10 m above the ground significantly decreased in the vicinity of onshore wind farm construction areas, while offshore wind farms also caused changes in sea surface temperature (SST). Pan et al.

Corresponding authors: Peng-Fei Tuo, tuopengfei@sz.tsinghua.edu.cn; Shengli Chen, shenglichen@sz.tsinghua.edu.cn

DOI: 10.1175/JAMC-D-23-0160.1

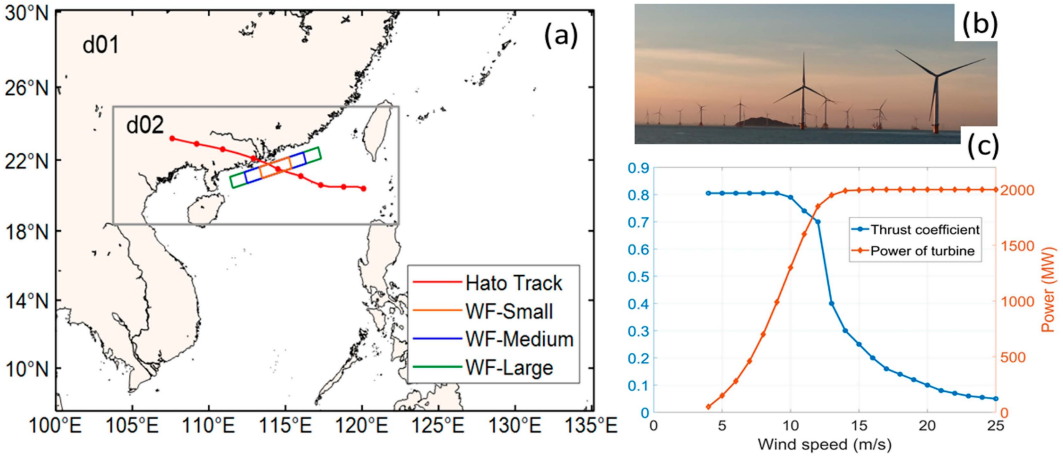

FIG. 1. (a) Domain of the simulation region, track of Hato, and wind farm layout in this study. The d01 and d02 are the outer and inner domains for the two-way nested grid system. The small (orange), medium (blue), and large (green) boxes denote the three different spatial sizes of the offshore wind farms in this study. (b) Photo of the wind turbine in the region of d02. (c) Wind turbine power and thrust coefficients are plotted against the wind speed for the 2-MW reference turbine. The reference turbine features a hub height of 75 m and a rotor diameter of 85 m. Due to the operational limits of the turbine, power production initiates at 4 m s^{-1} and ceases for wind speeds exceeding 25 m s^{-1}.

(2018), using the Weather Research and Forecasting (WRF) Model, studied the impact of different offshore wind farm layouts on precipitation during Hurricane Harvey using the wind farm parameterization scheme proposed by Fitch et al. (2012) and the increased surface roughness scheme proposed by Keith et al. (2004). Their results showed that coastal wind farm layouts could alter precipitation distribution during hurricane landfall, with increased precipitation upstream of the wind farms and reduced precipitation on the inland side.

Guangdong Province of China has a vast coastline in the northern part of the SCS. In the future, more large-scale offshore wind farms will be installed in the eastern region of Guangdong. The impact of these wind farms on the atmospheric and marine environment and extreme weather systems such as typhoons is unclear. In this study, we study the potential impacts of large-scale offshore wind farms on tropical cyclones, using Typhoon Hato as a case study. We first simulate the typhoon process using the WRF Model and validate the simulation results against observational data. We then study the effect of offshore wind farms on the intensity and precipitation during Hato. In addition, a series of sensitivity experiments are conducted to examine influencing factors such as the spatial size of offshore wind farms and variations in turbine spacing on typhoons. Here, the turbine spacing means the distance between two turbines in the wind farm. The paper is organized as follows: the model configuration and validation are given in section 2. Numerical model results and analysis are presented in detail in section 3, followed by a summary in section 4.

2. Model configuration, validation, and statistical significance testing

a. *Model configuration and validation*

We use the WRF Model to investigate the impacts of large-scale offshore wind farms on typhoon systems with version 4.2.2 of the model (Skamarock et al. 2019). In our WRF simulation, the GNU (gfortran/gcc) compiler is used to compile the model. The selected case for this study is Typhoon Hato, which formed in the northwest Pacific on 20 August 2017 and rapidly intensified. At 0700 UTC 22 August, it developed into a typhoon and eventually landed on the southern coast of Zhuhai City, Guangdong Province, at 0700 UTC 23 August. Near the coast region, Hato rapidly intensified and was accompanied by astronomical tides, resulting in severe storm surge disasters over the coastal areas. The model computational domain is shown in Fig. 1a. A two-way nested grid system is used with an outer grid resolution of 9 km and an inner grid resolution of 3 km. Vertical discretization is achieved by utilizing 50 layers, with the top layer at 50 hPa. We use the National Oceanic and Atmospheric Administration (NOAA) National Centers for Environmental Prediction (NCEP) final (FNL) analysis product (NCEP/National Weather Service/NOAA/US Department of Commerce 2000) for the initial and boundary conditions. In the simulation, SST data from NCEP FNL are updated every 6 h in this study. The simulation period is from 0000 UTC 22 August 2017 to 0000 UTC 24 August 2017, covering 48 h and comprehensively capturing the entire process of the typhoon landfall. The observational data on the track and intensity of Hato from the China Meteorological Administration (CMA) (Lu et al. 2021; Ying et al. 2014) are used to validate the results obtained from the simulations.

The WRF Model provides a variety of parameterization schemes. In this study, we configure the microphysics, cumulus convection, and planetary boundary layer schemes based on insights gleaned from previous studies (Fitch et al. 2012; Moon et al. 2021; Potty et al. 2012; A. Zhang et al. 2019; Z. Zhang et al. 2019). Specifically, our choices for microphysics schemes encompass the Lin scheme (Chen and Sun 2002), WSM3 (Hong et al. 2004), and WSM5 (Hong et al. 2006). For the cumulus convection schemes, the considered schemes in

TABLE 1. The WRF Model configuration for the combination of physical parameterization schemes. The first group (experiments 1–3) controls the microphysics scheme (i.e., WSM3, WSM5, and Lin), the second group (experiments 4–6) controls the cumulus convection scheme (i.e., KF, BMJ, and GD), and the third group (experiments 7–9) shares the same CTRL as the second group but employs different PBL schemes (i.e., YSU and MYJ).

Combination group	Microphysics	Planetary boundary layer	Cumulus convection
1	WSM3	YSU	KF
2	Lin	YSU	KF
3	WSM5	YSU	KF
4	Lin	YSU	KF
5	Lin	YSU	BMJ
6	Lin	YSU	GD
7	Lin	MYJ	KF
8	Lin	MYJ	BMJ
9	Lin	MYJ	GD

this study include the Betts–Miller–Janjić scheme (BMJ; Wang and Seaman 1997), the Kain–Fritsch (KF) scheme (Kain and Fritsch 1990), and the Grell–Devenyi (GD) scheme (Grell and Dévényi 2002; Grell and Freitas 2014). As for planetary boundary layer schemes, the Yonsei University (YSU) scheme (Hong et al. 2006) and the Mellor–Yamada–Janjić (MYJ) scheme (Janjić 1994) are employed.

The combination of parameterization schemes significantly influences the simulation results in simulating typhoons, and the optimal parameterization scheme varies for different typhoons. Prior to the control simulation, we conducted sensitivity experiments to identify the most suitable parameterization scheme combination for Typhoon Hato. Microphysics, cumulus convection, and planetary boundary layer schemes play crucial roles in simulating typhoons' precipitation, developmental processes, and the atmospheric structure's interaction with the land/ocean surface. Therefore, nine different parameterization combinations are designed for the simulation of Typhoon Hato, involving microphysics schemes WSM3, WSM5, and Lin; cumulus convection schemes KF, BMJ, and GD; and planetary boundary layer schemes YSU and MYJ. The specific parameterization combinations are detailed in Table 1. The experiments are divided into three groups: the first group (experiments 1–3) controls the microphysics scheme, the second group (experiments 4–6) controls the cumulus convection scheme, and the third group (experiments 7–9) shares the same control as the second group but employs different boundary layer schemes.

The results from experiments 1 to 3 (Figs. 2a,b), which employed different microphysics schemes for a 30-h simulation of Typhoon Hato with the YSU boundary layer and KF cumulus convection, showed varying simulation outcomes. Among these, the WSM3 microphysics scheme produced Typhoon Hato's track closer to observations but with a weaker intensity (Figs. 2a,b). The Lin and WSM5 schemes exhibited better results in terms of atmospheric pressure, with Lin simulating the lowest central pressure, closely resembling the observation from the CMA.

Upon selecting the Lin microphysics scheme and YSU boundary layer scheme for experiments 4–6 (Figs. 2c,d), and MYJ boundary layer scheme for experiments 7–9 (Figs. 2e,f), the simulation results indicated that the MYJ boundary layer scheme produced a stronger Typhoon Hato's intensity compared to the YSU scheme. Overall, the MYJ scheme performed better, especially regarding minimum sea level pressure, aligning closely with observed values. Under YSU boundary layer conditions, the GD cumulus convection scheme resulted in the strongest Typhoon Hato's intensity, while the KF and BMJ schemes produced similar intensities, weaker than GD. For MYJ boundary layer conditions, the choice of cumulus convection scheme did not significantly affect the simulation results.

The results from the sensitivity simulations reveal distinct influences of various parameterization schemes on Typhoon Hato simulations. First, the microphysics scheme emerges as a critical factor, significantly affecting the simulated track of Typhoon Hato. Among the microphysics schemes, WSM3 performs better in accurately representing Typhoon Hato's trajectory. Second, regarding boundary layer schemes, the MYJ scheme consistently outperforms the YSU scheme, especially in accurately simulating sea level pressure associated with Typhoon Hato. Third, the impact of cumulus convection parameterization schemes on simulation outcomes is contingent upon the chosen boundary layer scheme. Specifically, under YSU boundary conditions, the GD scheme produces the highest intensity for Typhoon Hato. In contrast, under MYJ boundary conditions, the choice of cumulus convection scheme exhibits less pronounced differences in simulation outcomes. Consequently, based on the insights gained from these sensitive experiments, the WRF Model configuration and the major physical parameterization schemes, including microphysics, planetary boundary layer, and cumulus convection, are determined and summarized in Table 2.

Typhoon movement and development are primarily influenced by the large-scale background field, notably the subtropical high pressure system and the westerly belt in the northwest Pacific (Hirata and Kawamura 2014). In numerical simulations, different simulation domains contain varying background field information, and the resolution of computational grids affects the model's ability to resolve mesoscale atmospheric motions. To assess this, sensitivity experiments with diverse simulation regions and spatial resolutions were conducted before the control simulation. For experiment A, the outer model domain spans 7.73°–33.19°N, 99.67°–132.33°E, and the spatial resolution is 15 km. The inner domain covered 16.85°–24.78°N, 108.42°–119.82°E with a high spatial resolution of 3 km. As a reference, experiment B's coverage is larger than A's. The outer model domain ranged from 11.34°S to 53.21°N, 90.79°–149.21°E, with a spatial resolution of 27 km, and the

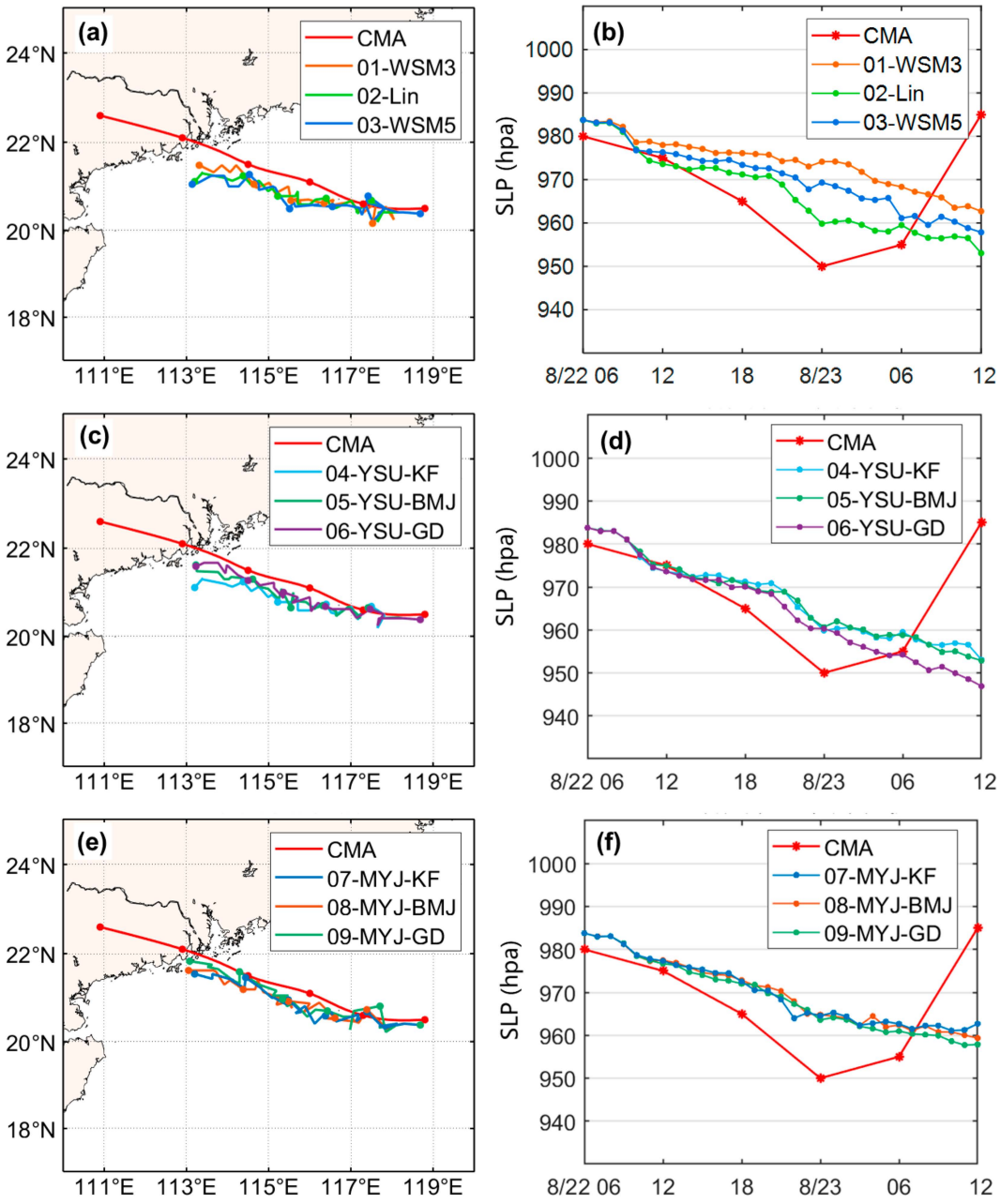

FIG. 2. (left) The observed and simulation of Hato's tracks and (right) intensity of sea level pressure in the center of Typhoon Hato. (a),(b) The first simulation group (Expt 1–3) controls the microphysics scheme (WSM3, WSM5, and Lin). (c),(d) The second group (Expt 4–6) controls the cumulus convection scheme (KF, BMJ, and GD). (e),(f) The third group (Expt 7–9) shares the same CTRL as the second group but employs different boundary layer schemes (YSU and MYJ). The red dotted lines in (a)–(e) indicate the observational Hato's track and intensity from the CMA. The simulation results are shown by the light blue, orange, and green lines.

inner domain covered 13.72°S–36.21°N, 105.44°–134.82°E with a spatial resolution of 27 km. Both experiments accurately simulated the track and intensity of Typhoon Hato. It is important to note that, for simplicity, figures have been omitted. In addition, because the typhoon track simulation result in experiment B is slightly better than that of A, the computational efficiency of experiment A is more than 10 times greater than that of experiment B, so based on the considerations of computing resources and efficiency, we choose the model simulation region of experiment A for subsequent experiments.

In this study, the horizontal resolution of the innermost grid is 3 km, much larger than the turbine spacing. We employ the wind farm parameterization scheme proposed by Fitch et al. (2012). This parameterization scheme considers

TABLE 2. The WRF Model configuration and major physical parameterization schemes.

Parameterization schemes	Domain01	Domain02
Lat/Lon	7.73°–33.19°N, 99.67°–132.33°E	16.85°–24.78°N, 108.42°–119.82°E
Horizontal grid resolution	9 km	3 km
No. of grid points	412 × 283	654 × 249
Timestep	30 s	10 s
Start and end time	0600 UTC 22 Aug–1200 UTC 23 Aug 2017	
No. of vertical layers	50	
Microphysics scheme	Lin (Chen and Sun 2002)	
Cumulus scheme	Kain–Fritsch (KF; Kain and Fritsch 1990)	
Planetary boundary layer	YSU (Hong et al. 2006)	
Longwave radiation scheme	RRTM (Mlawer et al. 1997)	
Shortwave radiation scheme	Dudhia (Dudhia 1996)	
Land surface model	Noah-LSM (Chen et al. 1996)	
PBL scheme	MYNN-2.5 (Nakanishi and Niino 2009)	
Surface layer scheme	MYNN (Nakanishi and Niino 2009)	

the effects of wind farms as momentum sinks and turbulence sources, which are incorporated into the calculations in the model boundary layer. Therefore, the influence of wind farms can be introduced to model simulations. The wind turbines used in this study have a rated power of 2 MW, a rotor diameter of 85 m, a hub height of 75 m, a cut-in wind speed of 4 m s^{-1}, and a cut-out wind speed of 25 m s^{-1}.

Before we simulate the influence of offshore wind farms on typhoons, it becomes imperative to consider the distinct effects arising from differing spatial dimensions of wind farms, which intricately interact with typhoon dynamics. We have used three different wind farm sizes (small, medium, and large) to answer this question. The central positions of each region are the same, and Typhoon Hato passes through the center of the wind farm in all simulation cases. The specific layout of the three sizes of regions is shown by colored boxes in Fig. 1a. The influence of the turbine spacing is also considered, and the wind turbine power and thrust coefficients are shown in Figs. 1b and 1c. We use the rotor diameter 85 m (represented by D) as the reference and design three different spacings: 14D, 10D, and 6D. Based on the wind turbine rotor diameter D, the turbine spacing values are 1190, 850, and 510 m in the three configurations.

The overall simulation design is summarized in Table 3. The experiment control (CTRL) represents the control model without the influence of wind farms. Experiments WF01–WF03 are conducted with a turbine spacing of 10D using the medium, small, and large sizes of the wind farm, respectively, to investigate the effects of different wind farm sizes for Hato. Meanwhile, experiments WF01, WF04, and WF05 are all conducted in the medium region and aimed to explore differences among turbine spacings of 10D, 6D, and 14D, respectively.

Figure 3 indicates a good agreement between the CTRL simulation and the observational data, effectively capturing the evolution of Hato both before and after landfall. First, the differences between the CTRL and CMA data regarding typhoon tracks, maximum surface wind speed at 10 m, and minimum sea level pressure are shown in Fig. 3. The maximum error within 48 h for the typhoon track is 87.2 km, with an average track error of 40.8 km (Figs. 2a,b). As for the typhoon intensity, the trends in the maximum wind speed and minimum sea level pressure are generally consistent with the CMA data (Figs. 2c,d). The error in maximum wind speed at 10 m is less than 6 m s^{-1}, and the maximum error in central pressure is approximately 20 hPa. All these results indicate that Hato's simulation accuracy in the CTRL simulation is excellent and similar to other research results (Moon et al. 2021).

Last, the Global Precipitation Measurement (GPM) dataset is used to validate the precipitation in CTRL. The GPM dataset has a temporal resolution of 0.5 h and a spatial resolution of 0.1° × 0.1°. The comparison between the accumulated precipitation in CTRL and the GPM satellite data is shown in Fig. 4. Regarding the precipitation distribution, the areas of heavy precipitation are predominantly located on the left side of the typhoon track. In the 6 h before typhoon landfall (Figs. 4c,d), the GPM satellite data indicate a concentrated precipitation area near the typhoon center, with no distinct rainbands in the outer region. However, the simulated precipitation areas are larger, with strong rainfall bands near the typhoon center and the outer periphery, resulting in a relatively scattered rainfall distribution. Regarding precipitation intensity, the accumulated rainfall in

TABLE 3. The design of the sensitivity study for the offshore wind farm spatial layout.

Exp	Wind farm size	Turbine spacings (m^{-1})	Turbine No.	Power (GW^{-1})
CTRL	—	—	—	—
WF01	Medium	10D = 850	41 650	83.30
WF02	Small	10D = 850	20 825	41.65
WF03	Large	10D = 850	62 050	124.10
WF04	Medium	6D = 510	114 100	228.20
WF05	Medium	14D = 1190	20 880	41.76

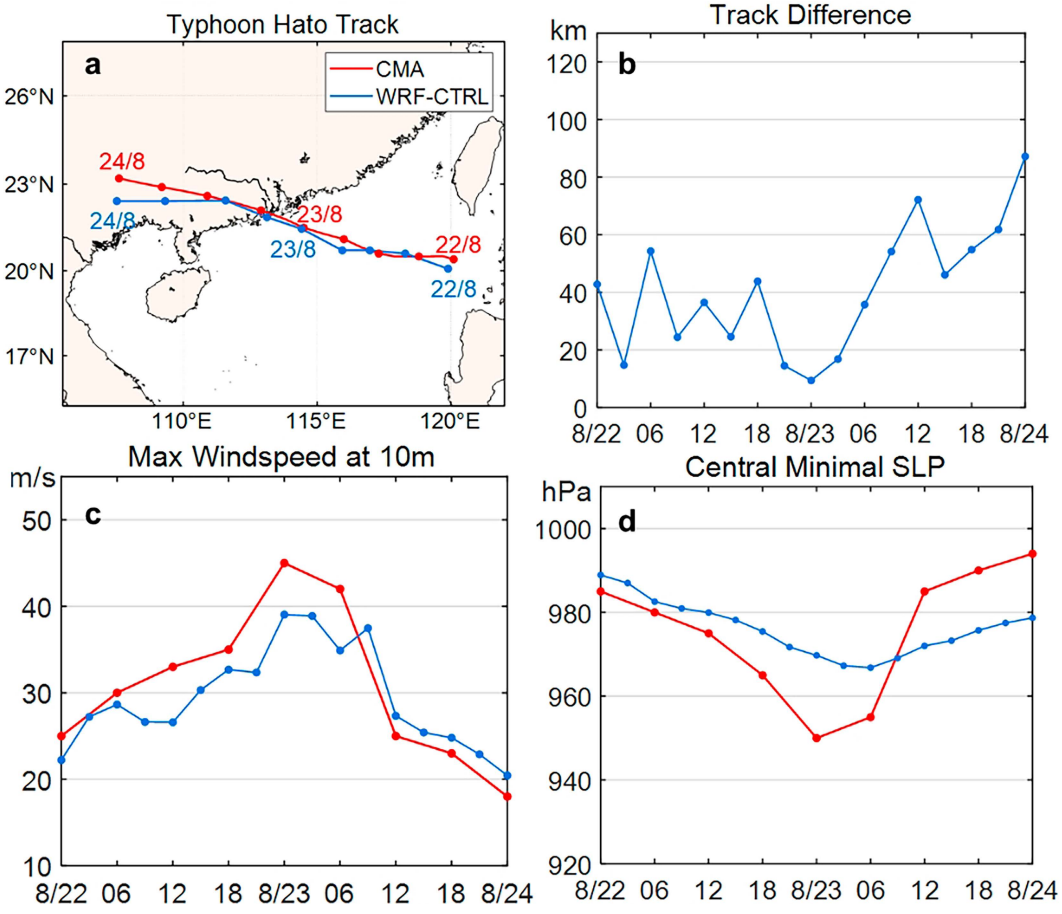

FIG. 3. Comparison between the simulation results and CMA reanalysis data. (a) The Hato's track, (b) track simulation errors, (c) maximum wind speed over 10 m, and (d) minimum sea level pressure. The CTRL simulation and CMA results are indicated by blue and red lines, respectively.

CTRL agrees well with the GPM satellite data, and the areas with heavy precipitation exceeding 150 mm in 6 h also exhibit good consistency. Overall, our CTRL simulation demonstrates a reasonable agreement regarding precipitation distribution and intensity with the observational data, capturing the spatial distribution and strength of precipitation during the typhoon period reasonably well.

b. *Statistical significance testing*

In our study, we utilize a nonparametric Monte Carlo bootstrapping method (Efron and Tibshirani 1994; Davison and Hinkley 1997; Wilks 2011) to rigorously assess the statistical significance of differences between observed meteorological changes across various model simulations. We selected this method for its flexibility and applicability to our dataset's characteristics. The nonparametric bootstrap, a resampling method, generates thousands of pseudosamples from the original dataset. It can estimate the sampling distribution for almost any statistic, providing a robust framework for significance testing that does not rely on traditional parametric hypotheses (Efron and Tibshirani 1994).

By resampling with replacement 10 000 times and computing the relevant statistic for each iteration, we construct an empirical distribution that reflects the statistic's variability under the null hypothesis. We derive confidence intervals and p values to quantify the significance of differences between control and sensitive simulations. The results from these bootstrap tests are crucial for framing our findings within the context of their statistical robustness. High statistical significance (p value < 0.05) would indicate a robust and reproducible effect of wind farms on meteorology, whereas low significance (p value > 0.05) would suggest that the observed meteorological changes could potentially occur randomly.

It is important to note that small sample sizes can produce low p values even for minimal differences, potentially leading to misleading indications of significance (Sprent and Smeeton 2016; Good 2005). Therefore, in cases with small sample sizes, we primarily relied on whether the confidence intervals from the data sampling overlapped to determine if there were significant differences. This approach ensures that our assessment of significance is more reliable and less likely to be influenced by the limitations of small sample sizes.

When assessing whether the differences between sensitivity experiments and control experiments are significant across the entire simulation region (Fig. 1a), we primarily conduct

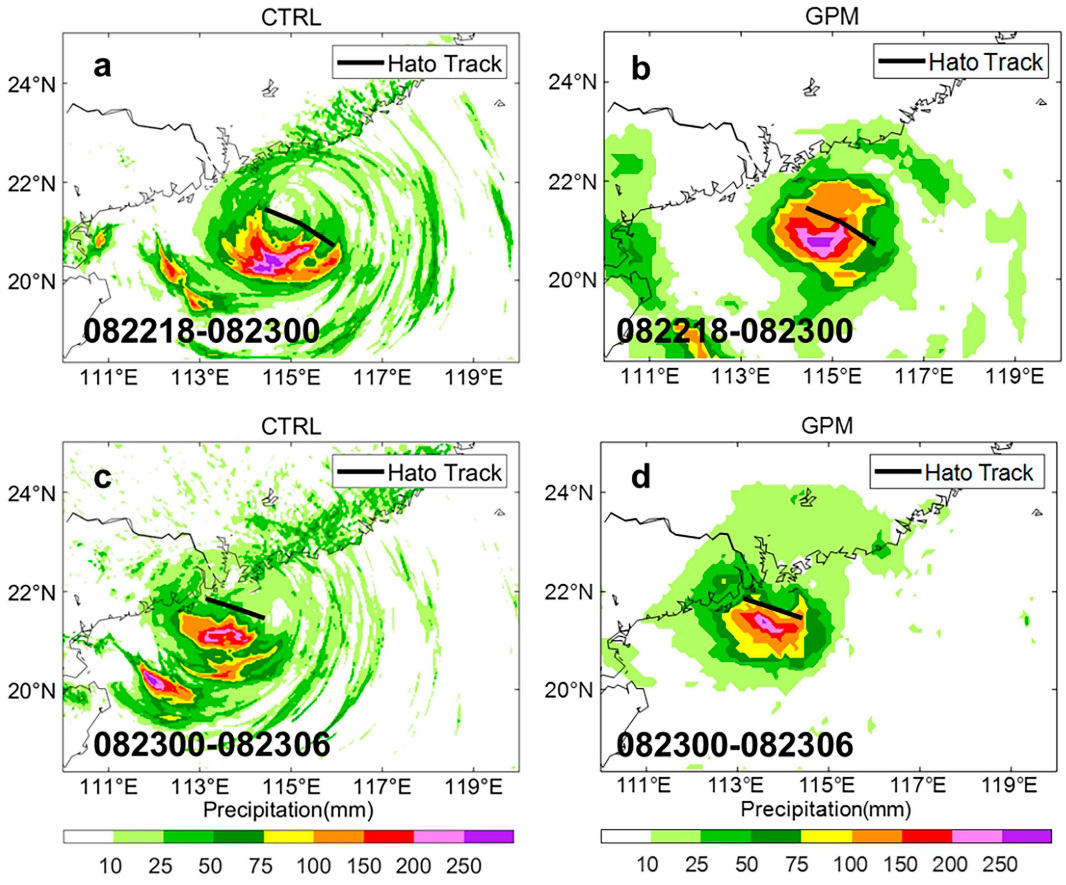

FIG. 4. Comparison of accumulated precipitation in 12 h [(a),(c) WRF-CTRL simulation results; (b),(d) GPM satellite data].

random sampling on the two-dimensional data fields of the region. However, when evaluating the significance of overall differences in the areas we selected (e.g., A, B, and C), we first calculate the overall average of the selected regions and then perform random sampling. This approach ensures that our assessment of significance takes into account both localized variations and overall regional trends, providing a comprehensive understanding of the meteorological impacts of wind farms.

c. *Rank-order nonparametric test*

Additionally, we employ a nonparametric rank-order test to determine the statistical significance of the rank-ordered simulation outputs (Sprent and Smeeton 2016; Good 2005). The rank-order test involves evaluating whether the observed simulation results fall into a meaningful rank order, which can indicate a significant trend or effect. For instance, with four well-ordered simulations (e.g., CTRL, small, medium, and large), there are 24 possible orderings, only two of which (1, 2, 3, 4 and 4, 3, 2, 1) correspond to the wind farm size determining the response size. In this study, we eventually tested three groupings for proper rank ordering: wind farm size, wind farm density (turbine number), and wind farm generation capacity.

This rank-ordering approach is a robust and flexible nonparametric method that does not assume a specific data distribution (Sprent and Smeeton 2016; Good 2005), making it particularly suitable for our analysis. By calculating the probability of obtaining the observed orderings under the null hypothesis, we can derive p values that indicate the statistical significance of the observed trends.

3. Impacts of offshore wind farms on Typhoon Hato

We take experiment WF01 (Table 2) as a reference run. All sensitivity simulations indicate that wind farms can cause a decrease in wind speeds on the near-surface and lead to a spatial variation in precipitation (cf. experiments WF01–WF03). The effect of wind farms with different spatial extents and turbine layout spacing are also investigated by a series of sensitivity experiments (cf. experiments WF01, WF04, and WF05).

a. *Attenuation of the wind speed*

Turbines operating within specific wind speed ranges convert the kinetic energy of wind into electrical energy, which will inevitably reduce local wind speeds. Compared to the results of experiment CTRL with that of WF01, it is evident that near-surface wind speeds decrease within the offshore

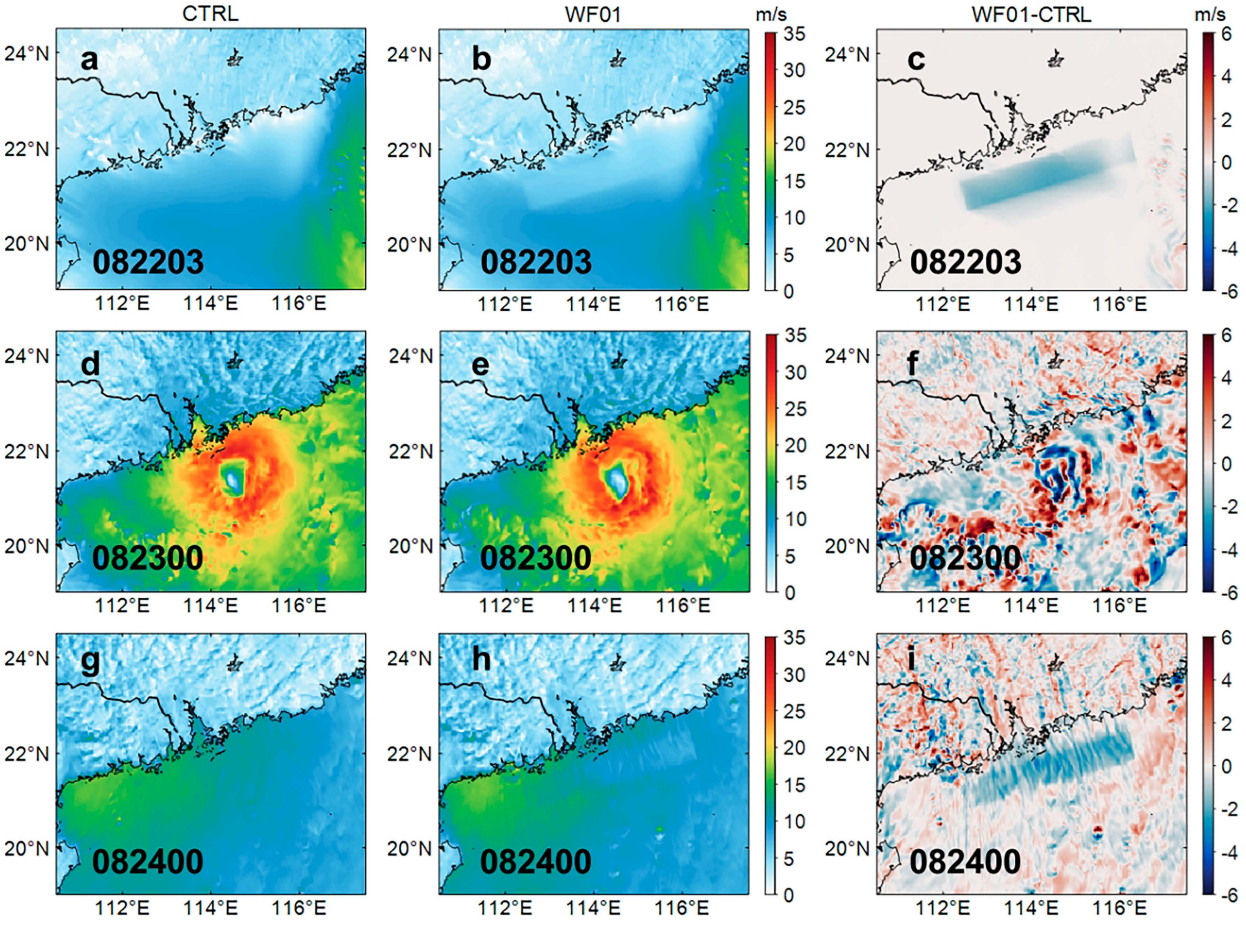

FIG. 5. Comparison and discrepancy of surface wind speed at 10-m locations during different times: (a),(d),(g) CTRL results; (b),(e),(h) WF01 experiments; (c),(f),(i) the difference between WF01 and CTRL. The corresponding time intervals in the figure are 0300 UTC 22 Aug, 0000 UTC 23 Aug, and 0000 UTC 24 Aug. The red pentagram denotes the position of the typhoon center.

wind farm area (cf. Figs. 5a,d,g and 5b,e,h). When the typhoon is located farther away from the wind farm and the ambient wind speeds are relatively low, a greater number of turbines within the wind farm can operate normally. In the results of WF01, a distinct area of wind speed attenuation can be significantly observed, as shown in Figs. 5c and 5i (p value < 0.05). The wind farms can reduce the wind speeds at the height of 10 m above ground level by 2–4 m s^{-1} compared with the results of the experiment without wind farms (CTRL). When the typhoon center is within or near the wind farm, most of the turbines within the wind farm stop operating due to wind speeds exceeding their cut-out speeds. In this case, no significant wind speed attenuation is observed within the wind farm, as shown in Fig. 5f. A comparison between Figs. 5d and 5e reveals that when Typhoon Hato passes through the wind farm, there are minimal changes in the intensity and structure of the near-surface wind field, as supported by a p value > 0.05, indicating that the differences are not statistically significant. The reduction in the overall intensity of the typhoon caused by the wind farm is limited.

Large-scale offshore wind farms can influence maximum wind speeds in coastal areas during typhoon events. It is crucial to note that during Typhoon Hato's landfall, the core wind speed exceeded 50 m s^{-1} (approximately 180 km h^{-1}), and the radius of strong winds (speeds greater than 20 m s^{-1}) extended beyond 100 km (Figs. 5d,e). Without wind farm effects (Fig. 6a), areas with high wind speeds are primarily located near the typhoon landfall location and to the right of the typhoon track, represented by regions A and B in Fig. 6. Wind speeds within these two regions generally exceed 15 m s^{-1}. Region A is near the typhoon landfall location, where the maximum coastal wind speed reaches 27 m s^{-1}. Region B is situated to the right of the typhoon track and is roughly parallel to the typhoon's movement. The maximum wind speed within this region is approximately 24 m s^{-1}, representing the central area of strong winds. If we take the wind speed of 16 m s^{-1} (orange-to-red areas) in Figs. 6a and 6b as a reference, it is evident that the warm-colored areas representing wind speeds in Fig. 6b have significantly shrunk compared to Fig. 6a. This observation indicates alterations in both the intensity and distribution of maximum wind speeds

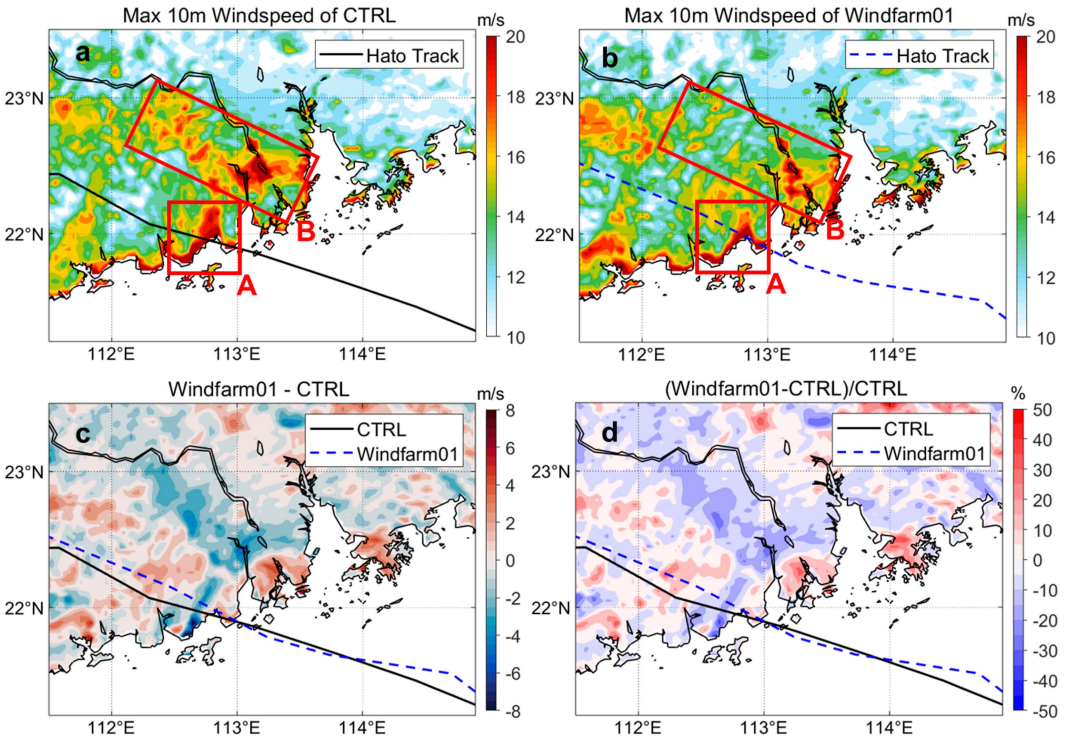

FIG. 6. Maximum wind speed and discrepancies at 10 m over the coastal land near the offshore wind farm.

within region B under the influence of the wind farm. This is characterized by a general decrease in maximum wind speeds and a reduction in the extent of the strong wind region. Simulation results indicate a significant reduction in the range of the high wind speed area to the right of the typhoon landfall location within region A, with wind speed decreases of 3–5 m s^{-1} (Fig. 6c) and a reduction of 8%–13% (p value < 0.05). In region B, the reduction in wind speeds is even greater, with maximum wind speed decreases of 2–5 m s^{-1} (Fig. 6d) and a reduction of 5%–24% (p value < 0.05). The region experiencing the most significant decrease (p value < 0.05) in the coastal land is located on the left side of the typhoon landfall location, specifically the lower left coastal area of region A, where the maximum wind speed decreases by 8 m s^{-1}, about 34% (p value < 0.05).

In addition to the decrease in maximum wind speeds in strong wind regions, there are also some areas where maximum wind speeds have increased. However, compared with the wind speed attenuation effects in regions A and B, the wind speed increase in these areas is smaller. The area experiencing increased wind speed comprises approximately 6% of region A and 11% of region B. Region A is centered precisely along the typhoon track, while region B is situated approximately 90 km from the typhoon center. Taking into account the overall changes in maximum wind speeds over the coastal land area, large-scale offshore wind farms have a mitigating effect on wind speeds in the coastal strong wind regions. Maximum wind speeds generally decrease by 2–5 m s^{-1}, with the highest reduction reaching 8 m s^{-1} (p value < 0.05), which can alleviate the severity of strong winds and the resulting disasters during typhoon events.

b. *Reduction of the precipitation in coastal areas*

Typhoon Hato's trajectory aligns with the conventional southeast-to-northwest track, akin to numerous preceding typhoons that have struck the Guangdong region. Under the influence of offshore wind farms, the precipitation during the typhoon landfall continues to be mainly concentrated on the left side of the track but with some variations in the distribution. The precipitation distribution in the outer rainbands of the typhoon shows minimal changes, whereas the intense rainfall area near the typhoon center undergoes noticeable variations. As the typhoon approaches and enters the offshore wind farm area (Figs. 7a,b), the offshore side of the wind farm experiences an accumulation effect, leading to increased precipitation ahead of the wind farm, as demonstrated in Fig. 7c with a statistical significance (p value < 0.05). After the typhoon passes through the wind farm and makes landfall (as illustrated in Figs. 7d,e), the intense precipitation zone shifts from the left side of the typhoon's original landfall location to within the wind farm area. While there is a decrease in precipitation for most of the coastal regions close to the landfall area, an increase in precipitation is observed over the southwest sea area of the wind farm (the southwest of the typhoon track), as we show in Fig. 7f, and this change is statistically significant (p value < 0.05).

Further calculations are conducted to investigate the water vapor flux divergence at the 850-hPa level, diagnose the

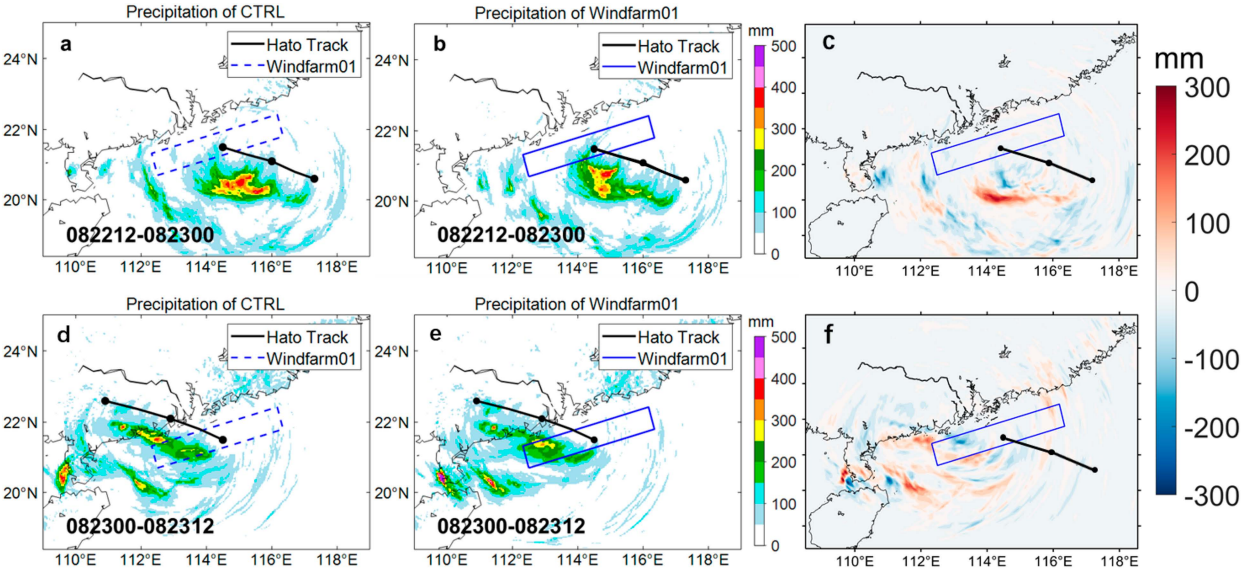

FIG. 7. Changes in precipitation distribution during Typhoon Hato (black solid line is the track from the simulation). (a),(b) The total rainfall over 12 h starting from 1200 UTC 22 Aug. (d),(e) The total rainfall during 12 h from 0000 UTC 23 Aug. (c),(f) The difference between WF01 and CTRL.

strength of the moisture convergence, and analyze the precipitation changes (as shown in Fig. 8). Generally, the divergence distribution of water vapor flux at the 850-hPa level is closely linked to precipitation patterns. Water vapor flux divergence reflects the horizontal transport of moisture within the atmosphere, and its distribution influences the spatial characteristics of precipitation. As moist air converges, it rises, cools, and condenses, forming clouds

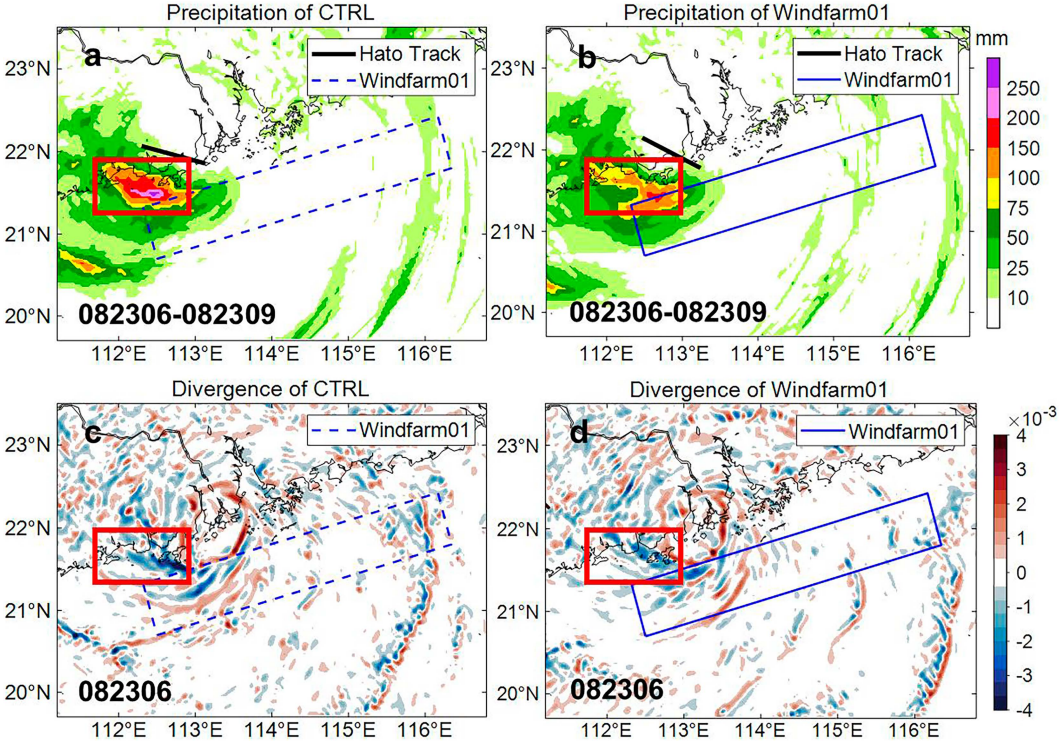

FIG. 8. Divergence of water vapor flux at the 850-hPa level and 3-h accumulated precipitation at 2100 UTC 22 Aug 2017 [(a),(b) water vapor flux divergence; 110^{-2} g $(cm^2 \cdot hPa \cdot s)^{-1}$, negative values indicate the water vapor convergence, and positive values indicate the divergence; (c),(d) 3-h accumulated precipitation; mm].

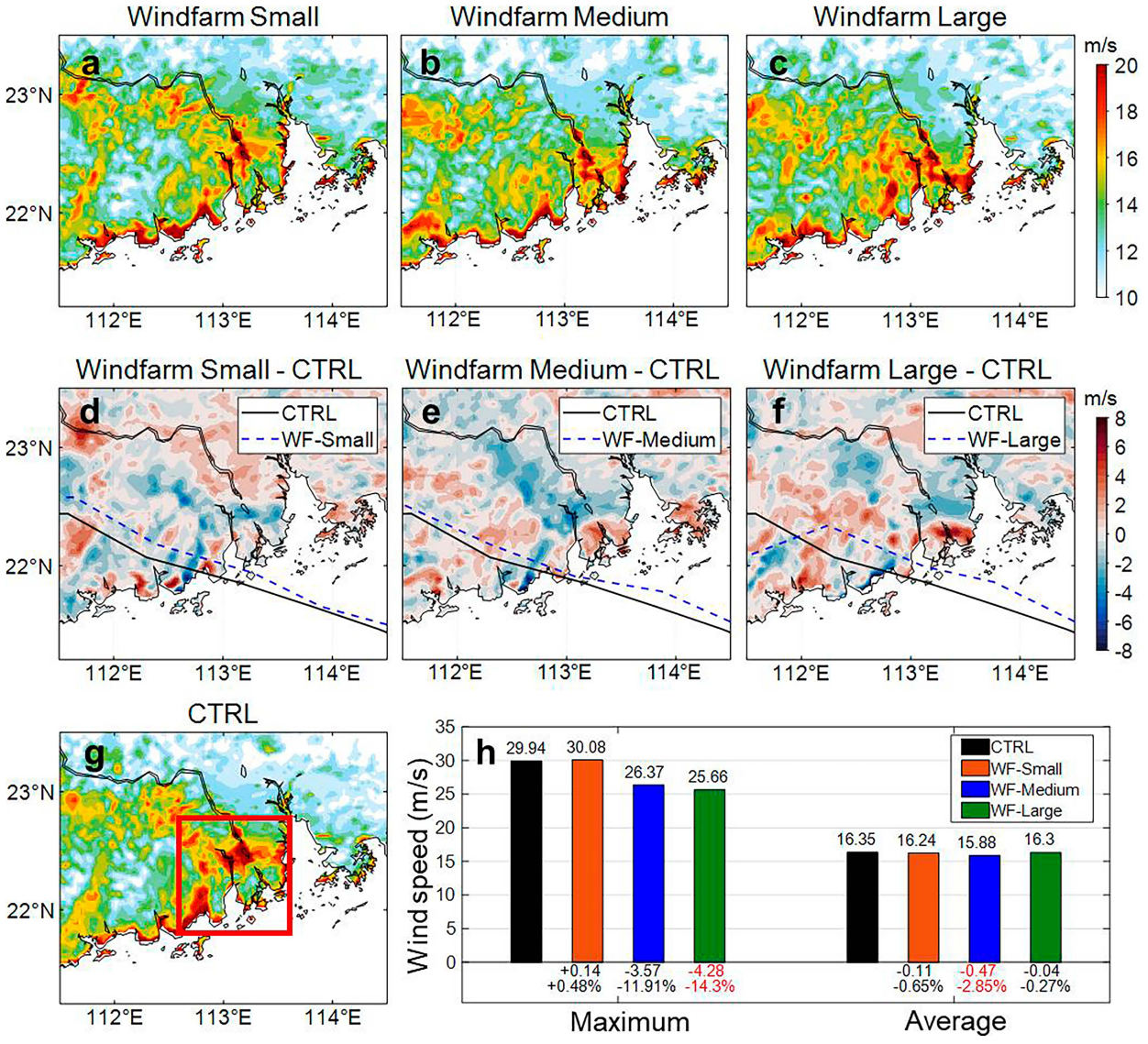

FIG. 9. Distribution of maximum 10-m wind speeds over the coastal land for different sizes of wind farms and their differences from CTRL. The red box in (g) represents the calculation range for maximum and area average wind speeds in 112.6°–113.6°E, 21.8°–22.8°N. (h) Differences in maximum wind speeds, average wind speeds, and their differences from CTRL near the landing location for different sizes of wind farms (the red values represent the maximum decrease in the wind speed and the corresponding percentage reduction).

and precipitation. Conversely, divergence in water vapor flux implies subsidence and drier conditions, inhibiting precipitation development.

During the typhoon's landfall, a discernible shift in the intensity and distribution of the rainfall center near the landfall location is observed. The presence of a wind farm introduces a notable impact, relocating the region of intense rainfall closer to the wind farm. This alteration is evident in the 3-h center area, where accumulated precipitation decreases from 150–250 to 100–150 mm, as depicted in Figs. 8a and 8b. Analyzing the divergence distribution of water vapor flux at the 850-hPa level reveals a correlation with the precipitation pattern. In the CTRL, negative divergence values are more pronounced and positioned closer to the coastline (cf. Figs. 8a,b). However, under the influence of the wind farm, these negative divergence values weaken and partially shift inward within the wind farm boundaries. This shift aligns with the observed changes in the intensity and distribution of the rainfall center. Consequently, large-scale wind farms exert a discernible influence on precipitation distribution by modifying low-level water vapor flux divergence. This results in reduced precipitation in coastal areas proximate to the typhoon's landfall region, as illustrated in Figs. 8e and 8d.

c. *Sensitivity study*

The distribution of maximum wind speeds over the coastal land and the differences in small, medium, and large sizes of wind farms from CTRL are shown in Figs. 9a–g. The

calculated results for the regional maximum wind speed and average wind speed for the three experimental groups compared with that of CTRL are also presented in Fig. 9h.

It can be observed that compared with the large size of the wind farm experiment, the landfall location of the typhoon deviates significantly from that of the CTRL, with the landfall location shifting further north (Figs. 9e,f). This increases the maximum wind speeds over the coastal land near the landing location, resulting in a limited reduction in average wind speeds near the original landing location. Figure 9h shows that the regional maximum wind speed increases by 0.14 m s^{-1} for the small size of the wind farm, with minimal change compared with that of CTRL. For medium- and large-size wind farms, the regional maximum wind speed decreases by 3.57 and 4.28 m s^{-1}, respectively, with 11.91% and 14.3% reductions in percentages. The larger the spatial size of the wind farm, the more significant the reduction in maximum wind speeds. In terms of average wind speeds, the small, medium, and large sizes of wind farms result in reductions of 0.11, 0.47, and 0.04 m s^{-1}, respectively, indicating a relatively small overall reduction in average wind speeds by the wind farms.

Following the detailed analysis presented in Fig. 9, we further quantified the statistical significance of the maximum 10-m wind speed differences between the controlled simulation and sensitivity simulations to ascertain the impact of the wind farm size on typhoon behavior. The nonparametric Monte Carlo bootstrap method was employed to compare each pair of simulation experiments, including CTRL, WF-small, WF-medium, and WF-large configurations. Due to the limited sample size shown in Fig. 9g (red box area), all comparisons yielded p value < 0.05 for both mean and variance, indicating statistically significant differences across all simulations. This uniform suggests that relying solely on p values for significance judgment may not be appropriate given the sample size limitations. Therefore, we assessed significance based on whether the 95% confidence intervals of the resampled data overlapped.

It is generally considered that if two confidence intervals do not overlap, there is a statistically significant difference between the two parameters at a given significance level (usually 5%) (Good 2005; Sprent and Smeeton 2016).

To provide a more rigorous assessment, we extended our analysis by calculating the 95% confidence intervals for the differences in maximum 10-m wind speeds. The bootstrap resampling analysis between the control experiment (represented by black lines in Fig. 10) and the wind farm configurations (represented by orange, blue, and red lines for WF-small, WF-medium, and WF-large, respectively) was performed. As shown in Fig. 10, the 95% confidence intervals indicate significant differences where the intervals do not overlap. Our results demonstrate no significant difference between the WF-large configuration and the control experiment. In contrast, both WF-small and WF-medium configurations show significant differences compared to the control. Furthermore, when comparing the sensitivity experiments horizontally, there is no significant difference between the WF-small and WF-medium configurations. These findings underscore the substantial influence of wind farm size on modifying regional wind speed dynamics, confirming the trends observed in Fig. 9. Notably, the shift in landfall location and the variations in

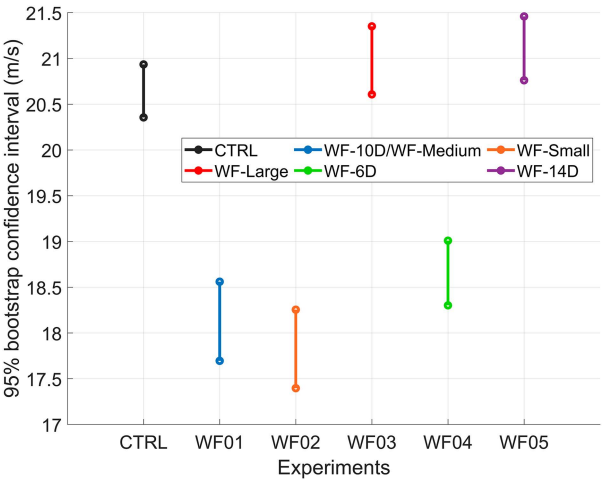

FIG. 10. Nonparametric Monte Carlo bootstrap confidence intervals for simulation experiments. The bars display the 95% confidence intervals for wind speed across different wind farm setups (CTRL, small, medium, and large) and turbine space (WF-6D, WF-10D, and WF-14D). Each interval is derived from 10 000 bootstrap samples, illustrating the variability and potential significance of differences between experimental setups. Overlapping intervals suggest nonsignificant differences, whereas nonoverlapping intervals indicate the significant differences at the 5% significance level.

maximum and average wind speeds across different wind farm sizes are visually apparent and supported by rigorous statistical analysis.

For wind turbine spacings of 14D, 10D, and 6D, the distribution of maximum 10-m wind speeds over the coastal land and their differences from CTRL are shown in Figs. 11a–g. The calculated results for the regional maximum wind speed and average wind speed for the three experimental groups compared with that of CTRL are presented in Fig. 11h. It is important to highlight that, for the convenience of comparing and statistically analyzing differences in typhoon physical characteristics among these various sensitivity experiments, we computed the time-averaged maximum wind speed and cumulative precipitation within the designated area centered around the typhoon. The size of this area is determined by the typhoon center, and the reported values represent averages over the specified period.

According to Figs. 11a–c, it can be observed that in the same wind farm area, the more densely the wind turbines are arranged, the lower the maximum wind speed near the typhoon's landfall. Under the 14D arrangement, the track after the typhoon landfall differs significantly from the CTRL scenario, resulting in changes in the distribution of maximum wind speeds over the coastal land (Fig. 11d). Additionally, with the sparse arrangement of wind turbines, there is no reduction in the wind speed. However, under the 10D and 6D arrangements (Figs. 10e,f), a reduction in the previously high wind speed areas can be observed, with a significant reduction of 10 m of wind over coastal land under the 6D arrangement.

Figure 11h shows the maximum wind speed and its average value in the vicinity of the landfall area for each experiment. Under the 14D arrangement, the maximum wind speed over

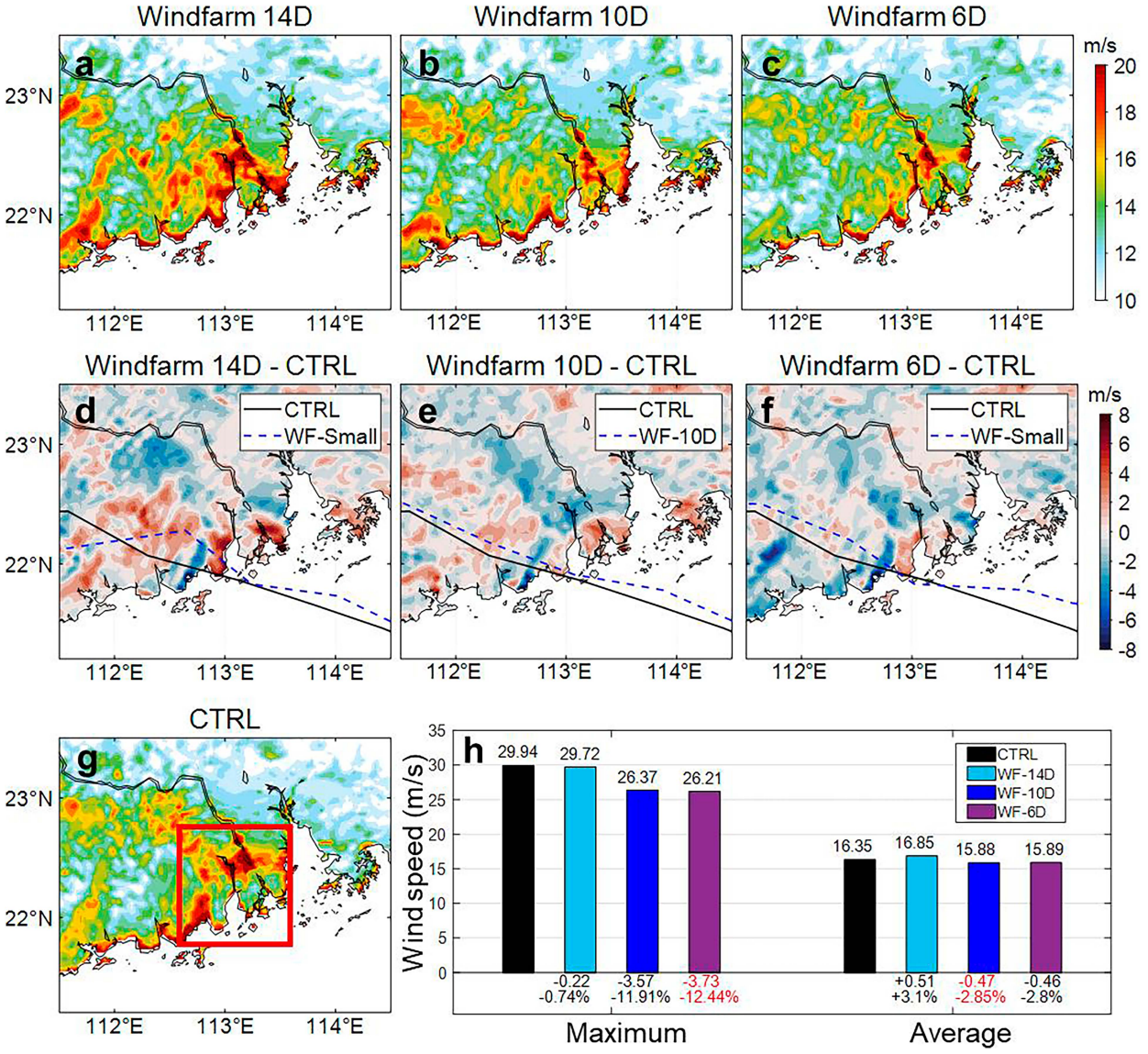

FIG. 11. Wind speed distribution at the maximum 10 m over the coastal land under various turbine spacing configurations and differences from CTRL [the red box in (g) indicates the range for calculating the average maximum wind speed near the landfall point]. (h) Maximum wind speed near the landfall location, mean wind speed, and discrepancies from CTRL under different turbine spacing (red values indicate the maximum reduction in the wind speed and the corresponding percentage decrease).

the coastal track has a relatively small impact, with only a decrease of 0.22 m s^{-1}. In contrast, under the 10D and 6D arrangements, there is a significant reduction in the maximum wind speed over the coastal land, with reductions of 3.57 and 3.73 m s^{-1}, respectively, representing a reduction of over 11%. Regarding the average wind speed, under the 14D arrangement, due to significant changes in the track after typhoon landfall, the average wind speed in the vicinity of the original landfall location increases by 0.51 m s^{-1}. The 10D and 6D arrangements reduce the average wind speed near the landfall point by 0.47 and 0.46 m s^{-1}, respectively. However, under the 6D arrangement, the reduction in the wind speed in the inland area is more pronounced, as shown in Figs. 11c and 11f.

Following the in-depth analysis of wind speeds and their distributions shown in Fig. 11, we conducted statistical tests to evaluate the significance of differences observed across various wind turbine spacing scenarios compared to the CTRL simulation results. The confidence intervals between CTRL (black bar) and WF-6D and 10D revealed significant differences in maximum and average wind speeds among the experiments (Fig. 10).

Interestingly, we found that when the turbine spacing was increased to 14D, the differences in the wind speed between the wind farm with 14D scenarios and the CTRL simulation were no longer statistically significant (Fig. 10). This observation is similar to our last section, where increasing the wind

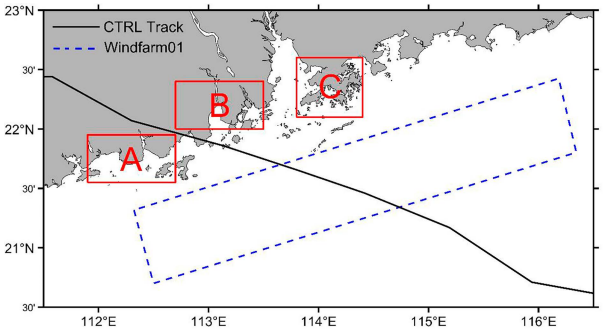

FIG. 12. Red boxes are the area-mean precipitation selected near the coastal region. The black line is the Hato track from the CTRL. The blue dot box is the layout of the wind farm.

farm size to WF-large resulted in a reduction in the differences between the experimental and control simulations.

We hypothesize that this result may be due to the increased spacing and size of the wind farm, leading to a more uniform impact on the simulated region (Ali et al. 2018; Stevens 2016). This uniformity likely averages out the global effects, thus diminishing the statistical significance of the differences. The increased dispersion of wind turbines may contribute to a more even distribution of their impact, reducing localized variations (Ali et al. 2018) and leading to a more homogeneous influence over the entire study area.

To further analyze the influence of wind farms of different sizes on precipitation in coastal areas during Hato, three regions, A, B, and C, as shown in Fig. 12, are selected to calculate the accumulated precipitation during the typhoon period. Among them, regions A and B are located on the left and right sides of the typhoon landfall point, respectively. In contrast, region C is selected as the coastal area close to the typhoon track, namely, Shenzhen–Hong Kong (Fig. 12). The average accumulated precipitation during the typhoon period for regions A, B, and C, as well as the overall average for the entire area, is shown in Fig. 13.

From Figs. 13a–d, it can be seen that during the typhoon period, precipitation is mainly concentrated after 0000 UTC 23 August. Before this time, the accumulated precipitation in each region is relatively small. Regarding regional distribution, precipitation is mainly concentrated on the left side of the typhoon track. In the CTRL experiment, the accumulated precipitation in area A reached 300 mm in 48 h, and the precipitation in the other three wind farm experiments exceeded 250 mm in 48 h. In contrast, the coastal areas on the right side of the typhoon track have less precipitation, with the highest average accumulated precipitation in areas B and C reaching 130 mm in 48 h.

Compared with the results of CTRL, the average accumulated precipitation in area A is reduced in all three wind farm experiments (Fig. 13e). The small size of the wind farm reduces the accumulated precipitation by 5.5%, while the large size reduces it by 15.8%. On the right side of the landfall point in area B, the small wind farm increases the average precipitation by 6.4%, while the medium wind farm shows the most significant decrease in precipitation, with a reduction of 31.3 mm, which is a decrease of 25.4%. All three experimental groups show a decline in precipitation in area C.

Overall, the small wind farm has a relatively small impact on precipitation, and the effects of precipitation increase or decrease vary in different regions. The medium and large sizes of wind farms significantly reduce the average precipitation in all three regions and are significantly lower than the small wind farms, but the difference between medium and large is insignificant.

The overall average accumulated precipitation in the entire region shows that wind farms' small, medium, and large sizes reduce the average accumulated precipitation by 5.3, 31.2, and 34 mm, respectively, in 48 h. The larger the wind farm area, the more significant the reduction in accumulated precipitation near the coastal areas adjacent to the landfall. From small to medium, as the wind farm area doubles, the percentage decrease in precipitation increases from 2.8% to 16.3%, showing a significant change. However, when the wind farm area increases to a large size, the average precipitation decreases by 2.8 mm compared with that of the medium-size wind farm.

In region A, the CTRL experiment demonstrates a significant difference in mean precipitation when compared to the WF-small, WF-medium, and WF-large simulations, as evidenced by the confidence interval bars in Fig. 14a. Both the mean and variance of accumulated precipitation in region A show statistically significant reductions in simulations testing sensitivity to wind farm size compared to the CTRL experiment. These findings indicate that larger wind farms substantially alter precipitation patterns to the left of the typhoon track, leading to a noticeable decrease in accumulated precipitation.

Conversely, in region B, located on the right side of the landfall point, both medium and large wind farm size setups reveal significant changes in accumulated precipitation compared to the CTRL simulation (Fig. 14b). Notably, the medium-sized wind farm simulation exhibits the most substantial reduction in accumulated precipitation, as depicted in Fig. 14b. This pattern is consistent with earlier observations of a shift in precipitation patterns, where larger wind farms contribute to a redistribution of precipitation across the coastal regions. The reduction in precipitation on the right side of the typhoon landfall suggests that wind farms can have asymmetric impacts on precipitation distribution, potentially affecting water availability in this area.

Region C, which represents the coastal area close to the typhoon track, specifically around the Shenzhen–Hong Kong region, also exhibits significant decreases in accumulated precipitation across all simulations compared with the CTRL, as shown in Fig. 14c. This underscores the broader impact of wind farms on modifying precipitation patterns, affecting not just the immediate vicinity of the wind farm but also extending to adjacent coastal areas. The consistent decrease in precipitation across all wind farm scenarios highlights the pervasive influence of wind farms on regional hydrological cycles, which could have important implications for water resource management and coastal ecosystem sustainability.

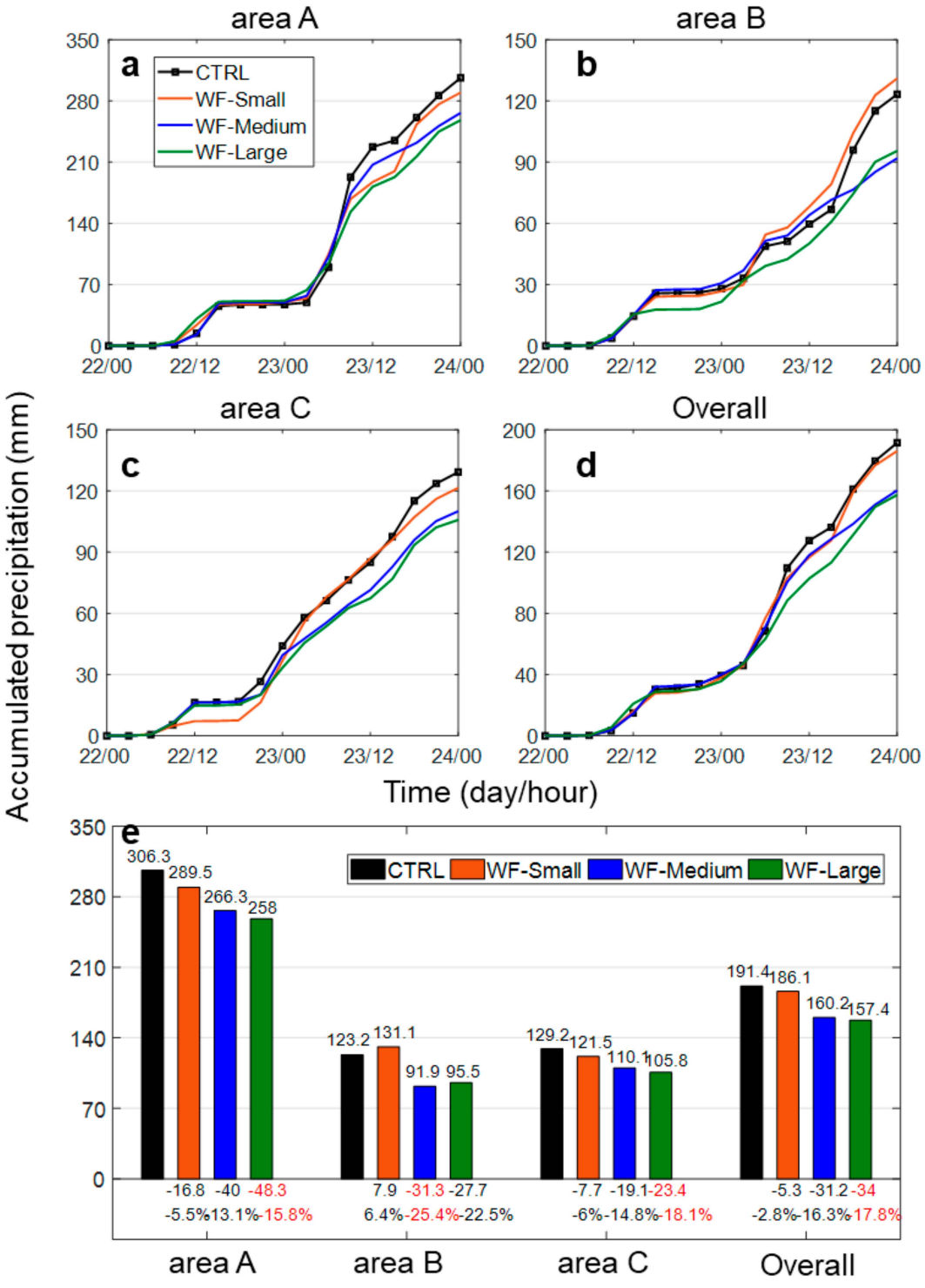

FIG. 13. (a)–(d) Average accumulated precipitation variation across different regions during typhoon events. (e) Average accumulated precipitation in different regions and differences from CTRL (red values indicate the maximum reduction in the accumulated rainfall and the corresponding percentage decrease).

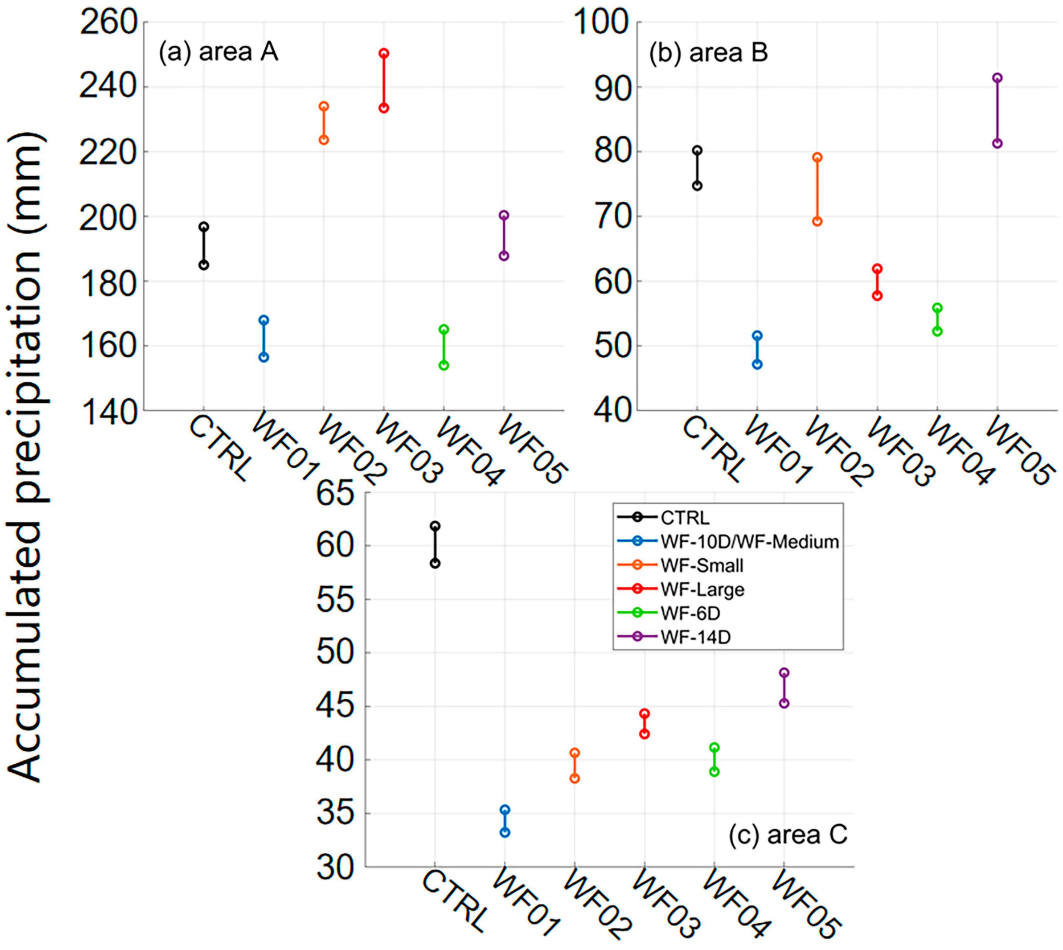

FIG. 14. As in Fig. 10, but for precipitation in areas A, B, and C.

Figures 15a–d show the impact of wind turbine spacing within medium-sized wind farms—specifically, spacings of 14D, 10D, and 6D—on the accumulated precipitation in coastal regions A, B, and C during Typhoon Hato. The results indicate that using a medium wind farm area with turbine spacing of 14D, 10D, and 6D leads to a reduction in average cumulative precipitation in coastal regions A, B, and C. Moreover, the denser the arrangement of turbines, the more significant the reduction in precipitation (cf. the black, blue, green, and purple confidence interval bars in Fig. 14). In the A region on the left side of the landing point, the 10D and 6D wind farms can reduce average cumulative precipitation by 13.1% and 14.4%, respectively. On the right side of the typhoon landing point in regions B and C, the 10D and 6D wind farms can decrease average precipitation by over 20%. As for the temporal distribution of precipitation, as shown in Fig. 15e, it is observed that the precipitation reduction caused by wind farms in regions A and B mainly occurs after the typhoon landing at 0600 UTC on the 23rd, while the precipitation reduction caused by the wind farm in region C starts as early as 0000 UTC on the 23rd. This is because region C is the coastal area of Shenzhen–Hong Kong, and Typhoon Hato moves from southeast to northwest. The moment when the typhoon is closest to region C is just before the landing. Therefore, the time when the average precipitation reduction in region C occurs is earlier compared with that of regions A and B.

In terms of the overall average for the entire area, the average values of 48-h cumulative precipitation decreased by 14.6, 31.2, and 34.8 mm with spacing arrangements of 14D, 10D, and 6D, respectively, corresponding to reduction percentages of 7.6%, 16.35%, and 18.2%. From 14D to 10D, the number of wind turbines in the wind farm approximately doubled, and the average rainfall decreased significantly from 14.6 to 31.2 mm. However, from 10D to 6D, although the number of turbines increased by approximately 1.7 times, the average rainfall decreased slightly from 31.2 to 34.8 mm, with a difference of only 3.6 mm. This indicates that reducing the turbine spacing beyond 10D has minimal marginal effects on reducing coastal precipitation.

d. Enhanced validation of sensitivity results

To enhance the robustness of our conclusions, we applied the rank-order nonparametric test to validate the significance of the results presented in Figs. 9h, 11h, 13e, and 15e (Table 4). This dual approach of using both the nonparametric Monte Carlo

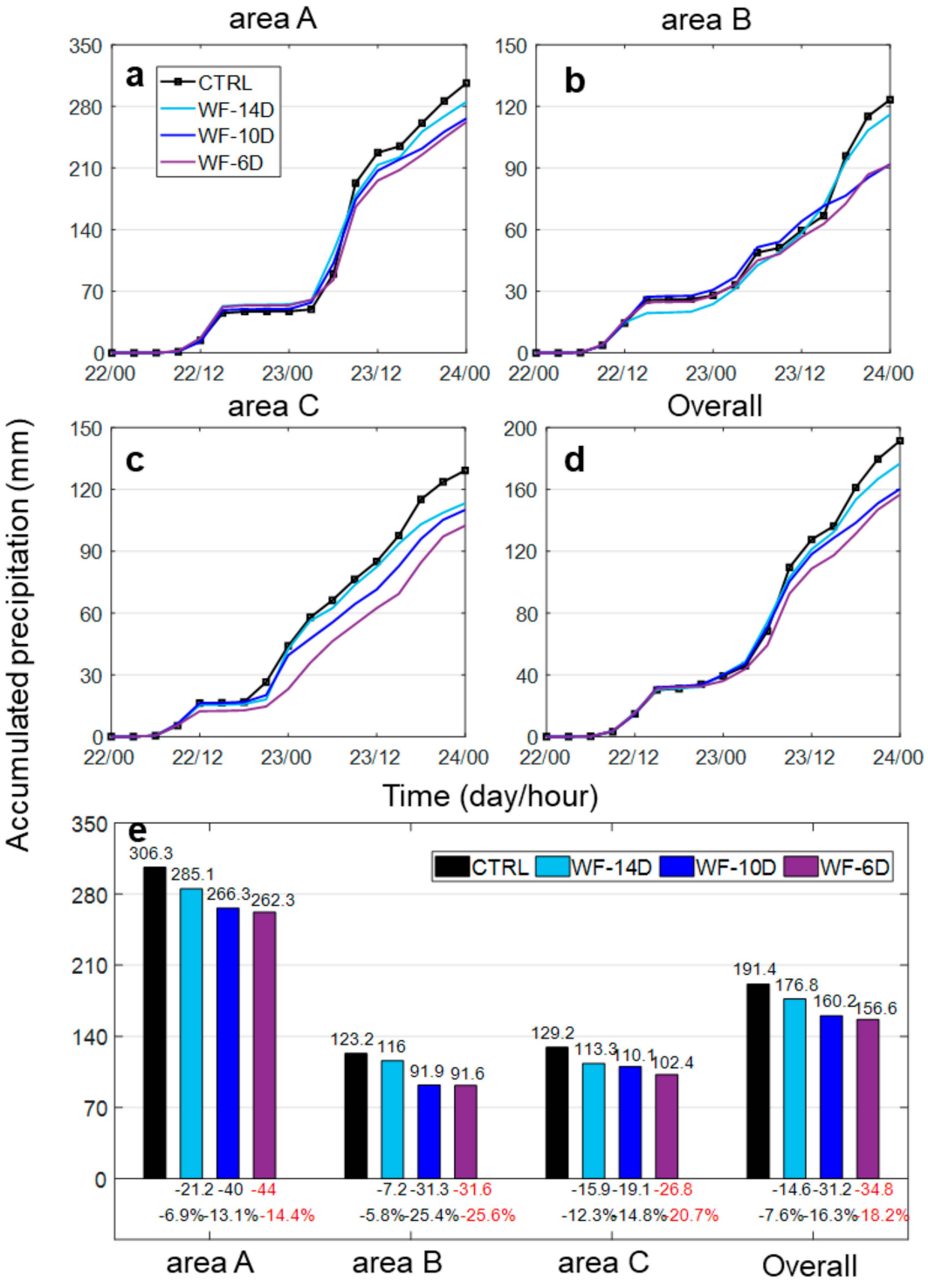

FIG. 15. The temporal evolution of average accumulated precipitation across different regions during the typhoon period (a)–(d). (e) The average accumulated precipitation across various regions and its deviation from the CTRL simulation (red values indicate the maximum reduction in the accumulated rainfall and the corresponding reduction proportion).

TABLE 4. Controlled and sensitivity simulation results for different wind farm configurations from Figs. 9h, 11h, 13e, and 15e. The table lists the experimental setup parameters and outcomes for the CTRL and five sensitivity experiments (WF01–WF05). Parameters include the wind farm size, turbine number, turbine spacing (reciprocal), and measured variables: maximum wind speed W_{max}, mean wind speed W_{mean}, and precipitation levels in three different areas (Precip A, Precip B, and Precip C) along with overall precipitation.

Expt	CTRL	WF01	WF02	WF03	WF04	WF05
Size	None	Medium	Small	Large	Medium	Medium
Name 1	CTRL	WF-medium	WF-small	WF-large		
Name 2	CTRL	WF-10D			WF-6D	WF-14D
Turbine No.	0	41 650	20 825	62 050	114 100	20 880
1/(Turbine spacing)	0	0.1	0.1	0.1	0.17	0.07
W_{max} (m s^{-1})	29.94	26.37	30.08	25.66	26.21	29.72
W_{mean} (m s^{-1})	16.35	15.88	16.24	16.3	15.89	16.85
Precip A (mm)	306.5	266.3	289.5	258	262.3	285.1
Precip B (mm)	123.2	91.9	131.1	95.5	91.6	116
Precip C (mm)	129.2	110.1	121.5	105.8	102.4	113.3
Precip overall (mm)	191.4	160.2	186.1	157.2	156.6	176.8

bootstrap test and the rank-order nonparametric test ensures a comprehensive and reliable analysis of the impact of wind farm configurations on regional climate variables.

We tested three groupings for monotonic rank ordering of the response: 1) wind farm size with four simulations: CTRL, WF-small, WF-medium, and WF-large (corresponding to Table 4: CTRL, WF02, WF01, and WF03); 2) wind farm density with four simulations: CTRL, WF-6D, WF-10D, and WF-14D (corresponding to Table 4: CTRL, WF01, WF04, and WF05); and 3) wind farm generation capacity with six simulations, with two of them being equivalent (corresponding to all experiments in Table 4).

Note here that for the six simulations, considering that two simulations have similar capacities (WF02 and WF04), the total number of possible orderings is adjusted to 6!/2 = 720/2 = 360. Out of these, there are only 24 monotonic orderings (either ascending or descending), so the probability of achieving a monotonic rank ordering by chance is 24/360 = 1/15.

Based on the three groups, we derived the following probabilities by random chance: 1) The chance of having at least one correct rank order (either ascending or descending) out of six simulations is 38%; 2) the approximate chance of having at least six correct rank orders out of nine simulations is 0.008%; and 3) the chance of having all three correct rank orders out of three simulations is 0.05%.

Subsequently, we examined the probability that various variables within the three monotonic rank-ordering groups—maximum wind speed W_{max}, mean wind speed W_{mean}, and precipitation levels in three different areas (Precip A, Precip B, and Precip C), along with overall precipitation—follow a monotonic rank-ordering pattern in Table 4. Our analysis revealed that sensitivity experiments involving wind farm size, wind farm density (turbine number), and wind farm generation capacity demonstrated a significant impact of wind farms on precipitation. However, when evaluated using the rank-order nonparametric test, the impact of wind farms on wind speeds during Typhoon Hato was less significant, contrasting with the results obtained from the nonparametric Monte Carlo bootstrap test.

This discrepancy may be attributed to the rank-order nonparametric test's assumption of a simple monotonic relationship between the wind farm size, turbine density, generation capacity, and typhoon wind speeds. In reality, these variables exhibit complex, nonlinear interactions with wind farm configurations.

Despite this, the additional analysis enhances the robustness of our assessment of the impact of wind farm configurations on regional climate variables.

4. Summary

We have developed a typhoon simulation model based on the WRF Model and used CMA and GPM data to verify the track of Typhoon Hato, central pressure, maximum wind speed, and accumulated precipitation. Numerical simulations incorporating a large-scale offshore wind farm are carried out. The results show that the wind speed at the ground level (10 m) in the wind farm area during the typhoon period can be reduced by 2–4 m s^{-1}, with a more pronounced effect observed at low wind speeds (environmental wind speeds of 10–15 m s^{-1}). Under the influence of the wind farm, the maximum wind speed near the landfall location over the coast can be reduced by 3–5 m s^{-1} in the strong wind region, and the area of the strong wind region is correspondingly reduced. In addition, the wind farm affects precipitation by influencing the atmosphere's low-level convergence. The area of heavy precipitation during the typhoon period moves from the coastal region toward the interior of the wind farm, resulting in a general decrease in precipitation in coastal areas.

Two sensitivity experiments are conducted to investigate the effects of wind farm sizes and different turbine spacing. The changes in coastal land wind speed and precipitation are compared with the simulation without the effects of wind farms. The results show that the maximum wind speed over the coastal region is reduced with the larger wind farm area and the smaller turbine spacing. Under a turbine spacing of 6D, the maximum wind speed over the coast can be reduced by 3.73 m s^{-1}, and the average maximum wind speed can be further reduced by 0.46 m s^{-1}. In all wind farm configurations, the average accumulated precipitation near the typhoon landfall is reduced. The larger the wind farm area and the denser

the turbine arrangement, the more significant the reduction in coastal average precipitation. Using a medium-sized area and a spacing of 10D can reduce the 48-h average accumulated precipitation near the landfall point over the coast by 31.2 mm, with a reduction ratio of 16%. However, further increasing the wind farm area or reducing the turbine spacing has limited effects on further reducing precipitation.

In this study, we used a 2 MW ideal turbine specification, but technological advancements show a clear trend toward larger turbine capacities. In 2021, China's average single-turbine capacity for offshore wind power reached 5.6 MW. Furthermore, the parameterization scheme for wind farms still has limitations and requires further optimization. Therefore, the individual case analysis in this study also has certain limitations, and further research on the topic is warranted.

Acknowledgments. This study was supported by funds from the Shenzhen Science and Technology Innovation Committee (WDZC20200819105831001) and the Guangdong Basic and Applied Basic Research Foundation (2022B1515130006). We extend our thanks to the three anonymous reviewers whose constructive feedback and invaluable suggestions have significantly enriched this manuscript, enhancing both its robustness and thoroughness. Additionally, we are deeply grateful to the editor, Dr. John W. Nielsen-Gammon, for his insightful suggestions, which have contributed significantly to our study.

Data availability statement. All observational data supporting this study's findings are presented in this manuscript. The CMA best track data (Lu et al. 2021; Ying et al. 2014) are accessed at https://tcdata.typhoon.org.cn/zjljsjj.html. The NCEP FNL data (NCEP/National Weather Service/NOAA/US Department of Commerce 2000) can be obtained from https://rda.ucar.edu/datasets/ds083.2/. The GPM data can be downloaded at https://gpm.nasa.gov/data/directory.

REFERENCES

Ali, N., N. Hamilton, D. DeLucia, and R. B. Cal, 2018: Assessing spacing impact on coherent features in a wind turbine array boundary layer. *Wind Energy Sci.*, **3**, 43–56, https://doi.org/10.5194/wes-3-43-2018.

Baidya Roy, S., and J. J. Traiteur, 2010: Impacts of wind farms on surface air temperatures. *Proc. Natl. Acad. Sci. USA*, **107**, 17 899–17 904, https://doi.org/10.1073/pnas.1000493107.

——, S. W. Pacala, and R. L. Walko, 2004: Can large wind farms affect local meteorology? *J. Geophys. Res.*, **109**, D19101, https://doi.org/10.1029/2004JD004763.

Cañadillas, B., and Coauthors, 2020: Offshore wind farm wake recovery: Airborne measurements and its representation in engineering models. *Wind Energy*, **23**, 1249–1265, https://doi.org/10.1002/we.2484.

Chen, F., and Coauthors, 1996: Modeling of land surface evaporation by four schemes and comparison with FIFE observations. *J. Geophys. Res.*, **101**, 7251–7268, https://doi.org/10.1029/95JD02165.

Chen, S.-H., and W.-Y. Sun, 2002: A one-dimensional time dependent cloud model. *J. Meteor. Soc. Japan*, **80**, 99–118, https://doi.org/10.2151/jmsj.80.99.

Davison, A. C., and D. V. Hinkley, 1997: *Bootstrap Methods and their Application*. Cambridge University Press, 582 pp.

Dudhia, J., 1996: A multi-layer soil temperature model for MM5. *Sixth PSU/NCAR Mesoscale Model Users Workshop 1996*, Boulder, CO, PSU/NCAR, 49–50, https://www.scirp.org/reference/referencespapers?referenceid=505238.

Efron, B., and R. J. Tibshirani, 1994: *An Introduction to the Bootstrap*. CRC Press, 456 pp.

Fiedler, B. H., and M. S. Bukovsky, 2011: The effect of a giant wind farm on precipitation in a regional climate model. *Environ. Res. Lett.*, **6**, 045101, https://doi.org/10.1088/1748-9326/6/4/045101.

Fitch, A. C., 2015: Climate impacts of large-scale wind farms as parameterized in a global climate model. *J. Climate*, **28**, 6160–6180, https://doi.org/10.1175/JCLI-D-14-00245.1.

——, J. B. Olson, J. K. Lundquist, J. Dudhia, A. K. Gupta, J. Michalakes, and I. Barstad, 2012: Local and mesoscale impacts of wind farms as parameterized in a mesoscale NWP model. *Mon. Wea. Rev.*, **140**, 3017–3038, https://doi.org/10.1175/MWR-D-11-00352.1.

——, J. K. Lundquist, and J. B. Olson, 2013: Mesoscale influences of wind farms throughout a diurnal cycle. *Mon. Wea. Rev.*, **141**, 2173–2198, https://doi.org/10.1175/MWR-D-12-00185.1.

Good, P. I., 2005: *Permutation, Parametric, and Bootstrap Tests of Hypotheses*. 3rd ed. Springer, 316 pp.

Grell, G. A., and D. Dévényi, 2002: A generalized approach to parameterizing convection combining ensemble and data assimilation techniques. *Geophys. Res. Lett.*, **29**, 1693, https://doi.org/10.1029/2002GL015311.

——, and S. R. Freitas, 2014: A scale and aerosol aware stochastic convective parameterization for weather and air quality modeling. *Atmos. Chem. Phys.*, **14**, 5233–5250, https://doi.org/10.5194/acp-14-5233-2014.

Hasager, C. B., P. Vincent, J. Badger, M. Badger, A. Di Bella, A. Penna, R. Husson, and P. J. H. Volker, 2015: Using satellite SAR to characterize the wind flow around offshore wind farms. *Energies*, **8**, 5413–5439, https://doi.org/10.3390/en8065413.

Hirata, H., and R. Kawamura, 2014: Scale interaction between typhoons and the North Pacific subtropical high and associated remote effects during the Baiu/Meiyu season. *J. Geophys. Res. Atmos.*, **119**, 5157–5170, https://doi.org/10.1002/2013JD021430.

Hong, S.-Y., J. Dudhia, and S.-H. Chen, 2004: A revised approach to ice microphysical processes for the bulk parameterization of clouds and precipitation. *Mon. Wea. Rev.*, **132**, 103–120, https://doi.org/10.1175/1520-0493(2004)132%3C0103:ARATIM%3E2.0.CO;2.

——, Y. Noh, and J. Dudhia, 2006: A new vertical diffusion package with an explicit treatment of entrainment processes. *Mon. Wea. Rev.*, **134**, 2318–2341, https://doi.org/10.1175/MWR3199.1.

IPCC, 2007: *Climate Change 2007: The Physical Science Basis*. S. Solomon et al., Eds., Cambridge University Press, 996 pp., https://books.google.co.in/books?id=8-m8nXB8GB4C.

——, 2014: *Climate Change 2013: The Physical Science Basis*. Cambridge University Press, 1535 pp., https://doi.org/10.1017/CBO9781107415324.

Jacobson, M. Z., C. L. Archer, and W. Kempton, 2014: Taming hurricanes with arrays of offshore wind turbines. *Nat. Climate Change*, **4**, 195–200, https://doi.org/10.1038/nclimate2120.

Janjić, Z. I., 1994: The step-mountain eta coordinate model: Further developments of the convection, viscous sublayer, and turbulence closure schemes. *Mon. Wea. Rev.*, **122**, 927–945,

https://doi.org/10.1175/1520-0493(1994)122%3C0927:TSMECM%3E2.0.CO;2.

Kain, J. S., and J. M. Fritsch, 1990: A one-dimensional entraining/detraining plume model and its application in convective parameterization. *J. Atmos. Sci.*, **47**, 2784–2802, https://doi.org/10.1175/1520-0469(1990)047%3C2784:AODEPM%3E2.0.CO;2.

Keith, D. W., J. F. DeCarolis, D. C. Denkenberger, D. H. Lenschow, S. L. Malyshev, S. Pacala, and P. J. Rasch, 2004: The influence of large-scale wind power on global climate. *Proc. Natl. Acad. Sci. USA*, **101**, 16 115–16 120, https://doi.org/10.1073/pnas.0406930101.

Knutson, T., and Coauthors, 2019: Tropical cyclones and climate change assessment: Part I: Detection and attribution. *Bull. Amer. Meteor. Soc.*, **100**, 1987–2007, https://doi.org/10.1175/BAMS-D-18-0189.1.

——, and Coauthors, 2020: Tropical cyclones and climate change assessment: Part II: Projected response to anthropogenic warming. *Bull. Amer. Meteor. Soc.*, **101**, E303–E322, https://doi.org/10.1175/BAMS-D-18-0194.1.

Knutson, T. R., and Coauthors, 2010: Tropical cyclones and climate change. *Nat. Geosci.*, **3**, 157–163, https://doi.org/10.1038/ngeo779.

Lauridsen, M. J., and B. C. Ancell, 2018: Nonlocal inadvertent weather modification associated with wind farms in the central United States. *Adv. Meteor.*, **2018**, 2469683, https://doi.org/10.1155/2018/2469683.

Lu, X., H. Yu, M. Ying, B. Zhao, S. Zhang, L. Lin, L. Bai, and R. Wan, 2021: Western North Pacific tropical cyclone database, created by the China Meteorological Administration. *Adv. Atmos. Sci.*, **38**, 690–699, https://doi.org/10.1007/s00376-020-0211-7.

Miller, L. M., and D. W. Keith, 2018: Climatic impacts of wind power. *Joule*, **2**, 2618–2632, https://doi.org/10.1016/j.joule.2018.09.009.

Mlawer, E. J., S. J. Taubman, P. D. Brown, M. J. Iacono, and S. A. Clough, 1997: Radiative transfer for inhomogeneous atmospheres: RRTM, a validated correlated-k model for the longwave. *J. Geophys. Res.*, **102**, 16 663–16 682, https://doi.org/10.1029/97JD00237.

Moon, J., J. Park, D.-H. Cha, and Y. Moon, 2021: Five-day track forecast skills of WRF model for the western North Pacific tropical cyclones. *Wea. Forecasting*, **36**, 1491–1503, https://doi.org/10.1175/WAF-D-20-0092.1.

Nakanishi, M., and H. Niino, 2009: Development of an improved turbulence closure model for the atmospheric boundary layer. *J. Meteor. Soc. Japan*, **87**, 895–912, https://doi.org/10.2151/jmsj.87.895.

NCEP/National Weather Service/NOAA/US Department of Commerce, 2000: NCEP FNL operational model global tropospheric analyses, continuing from July 1999. Research Data Archive at the National Center for Atmospheric Research, accessed 10 September 2021, https://doi.org/10.5065/D6M043C6.

Pan, Y., C. Yan, and C. L. Archer, 2018: Precipitation reduction during Hurricane Harvey with simulated offshore wind farms. *Environ. Res. Lett.*, **13**, 084007, https://doi.org/10.1088/1748-9326/aad245.

Peduzzi, P., B. Chatenoux, H. Dao, A. De Bono, C. Herold, J. Kossin, F. Mouton, and O. Nordbeck, 2012: Global trends in tropical cyclone risk. *Nat. Climate Change*, **2**, 289–294, https://doi.org/10.1038/nclimate1410.

Platis, A., and Coauthors, 2020: Long-range modifications of the wind field by offshore wind parks–results of the project WIPAFF. *Meteor. Z.*, **29**, 355–376, https://doi.org/10.1127/metz/2020/1023.

Possner, A., and K. Caldeira, 2017: Geophysical potential for wind energy over the open oceans. *Proc. Natl. Acad. Sci. USA*, **114**, 11 338–11 343, https://doi.org/10.1073/pnas.1705710114.

Potty, J., S. M. Oo, P. V. S. Raju, and U. C. Mohanty, 2012: Performance of nested WRF model in typhoon simulations over West Pacific and South China Sea. *Nat. Hazards*, **63**, 1451–1470, https://doi.org/10.1007/s11069-011-0074-4.

Schneemann, J., A. Rott, M. Dörenkämper, G. Steinfeld, and M. Kühn, 2020: Cluster wakes impact on a far-distant offshore wind farm's power. *Wind Energy Sci.*, **5**, 29–49, https://doi.org/10.5194/wes-5-29-2020.

Shepherd, T. J., R. J. Barthelmie, and S. C. Pryor, 2020: Sensitivity of wind turbine array downstream effects to the parameterization used in WRF. *J. Appl. Meteor. Climatol.*, **59**, 333–361, https://doi.org/10.1175/JAMC-D-19-0135.1.

Skamarock, W. C., and Coauthors, 2019: A description of the Advanced Research WRF Model version 4.3. NCAR Tech. Note NCAR/TN-556+STR, 165 pp., http://dx.doi.org/10.5065/1dfh-6p97.

Sobel, A. H., S. J. Camargo, T. M. Hall, C.-Y. Lee, M. K. Tippett, and A. A. Wing, 2016: Human influence on tropical cyclone intensity. *Science*, **353**, 242–246, https://doi.org/10.1126/science.aaf6574.

Sprent, P., and N. C. Smeeton, 2016: *Applied Nonparametric Statistical Methods*. CRC Press, 544 pp.

Stevens, R. J. A. M., 2016: Dependence of optimal wind turbine spacing on wind farm length. *Wind Energy*, **19**, 651–663, https://doi.org/10.1002/we.1857.

Walsh, K. J. E., and Coauthors, 2015: Hurricanes and climate: The U. S. CLIVAR working group on hurricanes. *Bull. Amer. Meteor. Soc.*, **96**, 997–1017, https://doi.org/10.1175/BAMS-D-13-00242.1.

——, and Coauthors, 2016: Tropical cyclones and climate change. *Wiley Interdiscip. Rev.: Climate Change*, **7**, 65–89, https://doi.org/10.1002/wcc.371.

Wang, Q., K. Luo, C. Wu, and J. Fan, 2019: Impact of substantial wind farms on the local and regional atmospheric boundary layer: Case study of Zhangbei wind power base in China. *Energy*, **183**, 1136–1149, https://doi.org/10.1016/j.energy.2019.07.026.

Wang, W., and N. L. Seaman, 1997: A comparison study of convective parameterization schemes in a mesoscale model. *Mon. Wea. Rev.*, **125**, 252–278, https://doi.org/10.1175/1520-0493(1997)125%3C0252:ACSOCP%3E2.0.CO;2.

Wilks, D. S., 2011: *Statistical Methods in the Atmospheric Sciences*. Vol. 100, Elsevier, 676 pp.

Ying, M., W. Zhang, H. Yu, X. Lu, J. Feng, Y. Fan, Y. Zhu, and D. Chen, 2014: An overview of the China Meteorological Administration tropical cyclone database. *J. Atmos. Oceanic Technol.*, **31**, 287–301, https://doi.org/10.1175/JTECH-D-12-00119.1.

Zhang, A., L. Xiao, C. Min, S. Chen, M. Kulie, C. Huang, and Z. Liang, 2019: Evaluation of latest GPM-Era high-resolution satellite precipitation products during the May 2017 Guangdong extreme rainfall event. *Atmos. Res.*, **216**, 76–85, https://doi.org/10.1016/j.atmosres.2018.09.018.

Zhang, Q., L. Wu, and Q. Liu, 2009: Tropical cyclone damages in China 1983–2006. *Bull. Amer. Meteor. Soc.*, **90**, 489–496, https://doi.org/10.1175/2008BAMS2631.1.

Zhang, Z., Y. Wang, W. Zhang, and J. Xu, 2019: Coastal ocean response and its feedback to Typhoon Hato (2017) over the South China Sea: A numerical study. *J. Geophys. Res. Atmos.*, **124**, 13 731–13 749, https://doi.org/10.1029/2019JD031377.